Experimental Study of the Flow Field in a Model 1.5-Stage Gas Turbine Rotor-Stator Disk Cavity

by

Nihal Junnarkar

A Thesis Presented in Partial Fulfillment
of the Requirements for the Degree
Master of Science

Approved November 2010 by the
Graduate Supervisory Committee:

Ramendra P. Roy, Chair
Taewoo Lee
Marc Mignolet

ARIZONA STATE UNIVERSITY

December 2010

ABSTRACT

A major concern in the operation of present-day gas turbine engines is the ingestion of hot mainstream gas into rotor-stator disk cavities of the high-pressure turbine stages. Although the engines require high gas temperature at turbine entry for good performance efficiency, the ingested gas shortens the lives of the cavity internals, particularly that of the rotor disks. Steps such as installing seals at the disk rims and injecting purge (secondary) air bled from the compressor discharge into the cavities are implemented to reduce the gas ingestion. Although there are advantages to the above-mentioned steps, the performance of a gas turbine engine is diminished by the purge air bleed-off. This then requires that the cavity sealing function be achieved with as low a purge air supply rate as possible. This, in turn, renders imperative an in-depth understanding of the pressure and velocity fields in the main gas path and within the disk cavities.

In this work, experiments were carried out in a model 1.5-stage (stator-rotor-stator) axial air turbine to study the ingestion of main air into the aft, rotor-stator, disk cavity. The cavity featured rotor and stator rim seals with radial clearance and axial overlap and an inner labyrinth seal. First, time-average static pressure distribution was measured in the main gas path upstream and downstream of the rotor as well as in the cavity to ensure that a nominally steady run condition had been achieved. Main gas ingestion was determined by measuring the concentration distribution of tracer gas (CO_2) in the cavity. To map the cavity fluid velocity field, particle image velocimetry was employed.

Results are reported for two main air flow rates, two rotor speeds, and four purge air flow rates.

ACKNOWLEDGMENTS

I wish to express my gratitude to Professor Ramendra P. Roy for his constant guidance and encouragement. I thank Professor Taewoo Lee and Professor Marc Mignolet for agreeing to be on my committee. I also would like to thank my colleague Jagdish Balasubramanian for his contribution to this work through his selfless involvement and helpful discussions. My thanks also extend to the personnel of Engineering Lab Services.

TABLE OF CONTENTS

LIST OF TABLES

TABLE PAGE

LIST OF FIGURES

NOMENCLATURE

b	outer radius of disk cavity
C	tracer (CO_2) gas concentration
C_{vax}	vane axial chord length
c_w	non-dimensional mass flow rate of purge air, = $\frac{\dot{m}_{purge}}{\mu b}$
$c_{w,fd}$	nondimensional free disk pumping flow rate, = $0.219Re_{\Phi}^{0.8}$
dT, ΔT	laser pulse separation time
$\dot{m}_{purge}$	mass flow rate of purge air (kg/s)
p	instantaneous static gage pressure
$\bar{p}$	time-average static gage pressure
p_{amb}	ambient pressure
Re_{vax}	main air flow Reynolds number, = $\rho V_{ax} C_{vax} / \mu$
Re_{Φ}	disk rotational Reynolds number, = $\rho \Omega b^2 / \mu$
s	axial gap between rotor and stator disks
V_{ax}	mixed-mean axial velocity of main air in annulus
β_2	angle, to axial direction downstream, of the main air velocity relative to the blade – at just downstream of vane trailing edge (^{o})
η	local sealing effectiveness

μ	dynamic viscosity (kg/m/s)
ρ	density of air (kg/m^3)
Ω	rotor disk speed
Φ	azimuthal coordinate

Chapter 1

INTRODUCTION

1.1 Background

Present day gas turbine engines have a much higher efficiency than the gas turbine engines introduced in the sixties. Key to this has been a dramatic increase in the mainstream hot gas temperature (to about 2000K). This increase in the main gas temperature has been made possible by the introduction of effective cooling and sealing of turbine internal components and also by the use of better materials for the components.

Figure 1.1 shows a schematic diagram of a typical sealing and cooling system in a gas turbine engine in reference to the mainstream gas flow. It is known that the temperature of the main gas flowing over the blades and vanes is above the melting point of the materials used to make the airfoils. This necessitates efficient cooling of the airfoils. Furthermore, if the main gas is ingested into the rotor-stator cavities of the turbine, overheating of the rotor disks may occur affecting the durability of the disks. To counter the ingestion of hot main gas into the cavities, seals are installed at the rotor disk and stator rims and purge air bled from the compressor discharge is injected into the cavities. The purge air is supplied at locations ranging from the rotor hub to radially outboard near the rim. The purge air may be supplied with or without pre-swirl; providing an appropriate amount of swirl to the purge air enhances the of the gas turbine engine performance.

It is important to understand however that bleed-off of air from the

compressor discharge reduces the overall performance of the gas turbine engine. Hence, the sealing and the cooling of the disk cavity internals should be achieved with the smallest possible amount of purge air. To achieve this, it is necessary to have detailed knowledge of the flow field within the rotor-stator disk cavities.

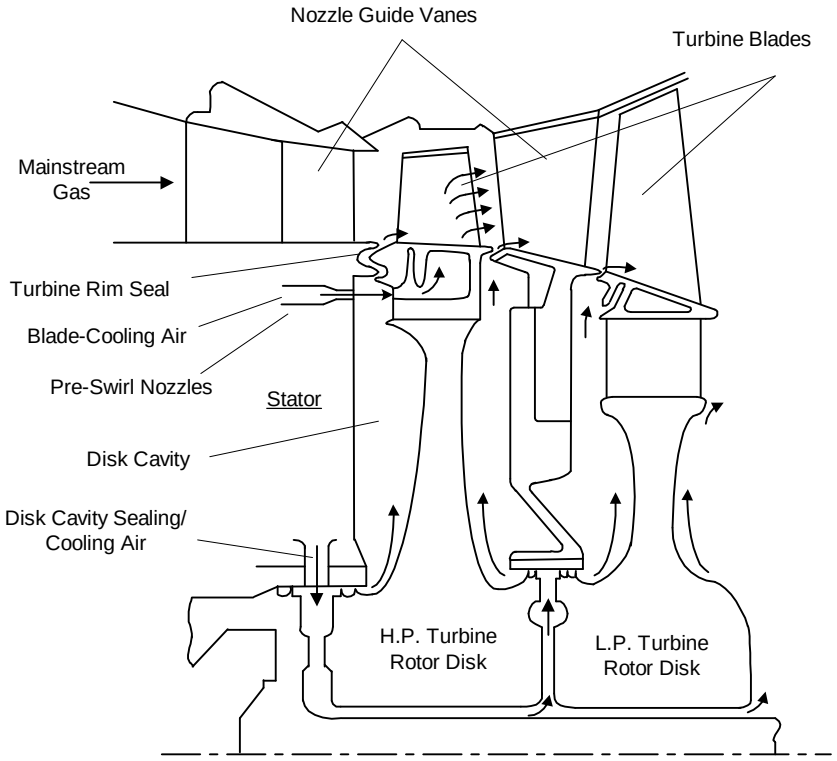

Fig. 1.1 A typical turbine cross-section with sealing and cooling air system (courtesy of Wilson et al., 1995)

1.2 Literature Survey

Gas flow in a turbine engine is a complicated process. Many works have been performed to understand the flow. Since our interest here is mainly in the main gas ingestion phenomenon and the associated flow in the main gas path and in the rotor-stator cavity, selected research papers both experimental and

theoretical/computational in scope are briefly discussed in this section.

Daily and Nece (1960) performed an experimental research to study the flow field due to rotation of a smooth plane disk enclosed within a right circular chamber. It was concluded in the paper that the flow field within the disk cavity depends solely on the rotational Reynolds number and the gap ratio, which is the ratio of the axial gap and the outer radius of the disk. They subdivided the flow regimes into four categories. The 3^{rd} and the 4^{th} category which featured turbulent flow is applicable to the experimental work described in this work.

Pressure, temperature, velocity and ingestion measurements experiments were performed by Abe et al. (1979). Propane tracer gas was used for the ingestion experiments. A 27 vanes stator disk with a β angle of 50° and a rotor with no blades were used for the experiments. The rotor and stator were provided with rim seals which had a radial clearance and an axial overlap. Ingestion measurements were taken at seven radial locations. At each radial location a 1 mm diameter stainless steel probe was traversed axially to make measurements in the axial direction. It was found that the ingestion was lower near the stator disk as compared to that near the rotor disk. Ingestion was found to be affected mainly by the ratio of the secondary air flow to the main gas flow rate, the rim seal radial clearance, and the rim seal axial overlap. It was, however, not affected by the disk rotational Reynolds number (Re_ϕ) when Re_ϕ was less than $1.0x10^6$.

Three main flow conditions; no main flow, quasi-axisymmetric main flow with no stator vanes and rotor blades and nonsymmetric main flow, were employed by Phadke and Owen (1988a, b, c) to visualize and measure pressure

and ingestion in a rotor-stator disk cavity for several rim seal configurations. A quantitative difference was found in the minimum secondary air flow rate required to prevent the ingestion, $c_{w,min}$, determined from the three flow conditions. Ingestion was found to be higher near the stator disk as compared to the rotor disk. They also postulated that the ingestion of main gas into the cavity could be rotationally dominated or main gas flow dominated.

Studies based on ingestion of main gas into the rotor-stator rim cavity for a gas turbine engine with both rotor blades and stator vanes are limited. In a recent study by Green and Turner (1994), they found that ingestion was lower when both the stator vanes and rotor blades were used instead of just stator vanes. Since, according to them, the blades forced the main flow downstream from the vanes more axisymmetric in the region of the rim seals.

Bohn et al. (2003) performed unsteady 2D LDV measurements in the cavity and the sealing gap of a 1.5 stage turbine engine to obtain the velocity distribution of the secondary and main gas path air. In was found that ingestion was high when a rotor blade passed a stator vane and also at lower secondary air flow.

Numerical simulations were performed on a 1.5 stage model gas turbine engine by Jakoby et. al. (2004) with axial seal (a seal lip in the periphery at either side) but no radial or axial overlap. The configuration consisted of two disk cavities; the front cavity and the back cavity The special focus of this study was to find large scale rotating structures (also found by Cao et.al 2003) in the front cavity which could cause ingestion. This phenomenon was captured with an

unsteady calculation using a 360 deg. computational domain since the structure cannot be captured using a sector mesh.

A large scale rotating structure that revolved with 80% of the rotor speed was detected in the front cavity, when the purge flow rate falls below a certain limit. This limit was found to be c_w = 15000. This number could however change with the seal configuration and with experimental conditions. The rotating structure in the rim cavity significantly influenced ingestion of mainstream gas into the front disk cavity.

Steady and unsteady CFD simulations were carried out by Gentilhomme et al. (2002) in a single-stage axial turbine rig. Time-average pressure distribution and ingestion were measured. From CFD studies, unsteady effects due to rotor blades were found to be key contributors to ingestion.

Cao et al. (2003) conducted an experiment using both CFD and experimental techniques to study the interaction between main gas path and purge flows. Experiments were conducted in a two-stage axial turbine rig. The CFD model was unsteady and its results on ingestion exhibited significant improvement over the corresponding steady computations. An unsteady flow feature in the radially outboard region of the cavity qualitatively similar to Bohn et al. (2000) was predicted by the CFD.

Roy et al. (1999, 2000, 2005) performed a thorough study to understand the fluid flow within a rotor-stator cavity. Unsteady as well as time averaged static pressure measurements in a model single stage axial flow turbine. Measurements were taken at various locations inside the rotor-stator disk cavity

and main gas path. The rotor was equipped with blades and the stator was equipped with vanes. Both had rim seals. CO_2 gas was used to measure ingestion at different axial locations in the disk cavity and on the stator surface. PIV experiments were performed to map a quadrant of the cavity. The velocity maps and the derived component velocities helped in understanding the nature of main gas path and cavity flows.

Unsteady 2D LDV experiments were performed by Bohn et. al. (2003) in the front cavity, inside the sealing gap, of a 1.5-stage axial flow turbine featuring 16 vanes (both the vane rows) and 32 blades, for different sealing air mass flow rates. Velocity measurements were taken at 2 radial locations (r/R = 0.985 and 0.952) and at 17 circumferential and 5 axial locations (for each radial location).

The flow-field inside the gap was seen to be influenced by the rotor blades and the guide vanes. Even for higher sealing air mass flow rates, (where an outflow of the sealing air flow was expected), hot gas ingestion occurred in the positions near the rotor blades. The higher pressure in-front of the blades seemed to cause this ingestion. The intensity of ingestion was seen to increase when the rotor blades passed by the stator wake. The region of hot gas ingestion was seen to move along with the rotor blade.

Decreasing the Sealing air mass flow intensified the main gas ingestion. At the radial location deeper within the cavity (r/R = 0.952), the velocity remained at a constant value over the circumference, indicating that the effect of rotor-passage and blade-vane interaction does not affect the velocity much deeper within the cavity.

Bohn et. al. (2006) performed experiments on a 1.5 stage model gas turbine. Two seal configurations were used in their experiments; an axial seal with seal lip in the periphery at either side and the radial seal with a seal lip in the periphery of the stator disk, overlapping a lower positioned seal lip of the rotor disk. Pressure and ingestion measurements were performed for both seal configurations and compared. It was found that the radial seal configuration performed better with a much higher efficiency than the axial seal due to the different type of rim seal.

Analysis on a 22.5 sector of the 1.5 stage gas turbine with stator vanes (16 vanes upstream and downstream of rotor blades) and rotor blades (32 blades) was performed by Rabs et. al. (2009). It was found from the pressure data that the Kelvin-Helmholtz instabilities were suppressed due to the presence of stator vanes and rotor blades. For high secondary gas flow rate (c_w = 30000), pressure distribution in the mainstream gas path direction shows that a low pressure region develops in the gap (between the stator rim and the rotor rim) area. This low pressure region indicates a vortex structure initialized by the Kelvin-Helmholtz instability. From velocity vector plots it was found that the vortex turns radially inwards at the rotor wall and radially outward at the stator wall indicating that the mainstream gas is ingested into the cavity from the rotor side and the secondary gas egresses from the stator side.

1.3 Overview of this work

In our experiments, it was of utmost importance to keep the basic features

of a gas turbine engine such as rotor blades, stator vanes, and seals on both the rotor disk and stator rims. Even though the rotor-stator configuration used is simpler than in an actual gas turbine engine, the study is capable of providing better understanding of the flow field.

The remainder of this thesis is organized as follows.

Chapter 2 provides a description of the experimental facility, the turbine stage, the measurement techniques, and procedures followed for measuring the time-average static pressure, time-average ingestion, and instantaneous/ ensemble-averaged velocity field in the disk cavity.

Chapter 3 contains the experimental results and their discussion.

Finally, Chapter 4 summarizes the conclusions of the present study.

Chapter 2

THE EXPERIMENTS

2.1 Experimental Facility

Three main components of the experimental facility are; the main blower, the secondary blower and the rotor motor. Each is described briefly in the following section.

Main Blower

A centrifugal blower (22.4 kW, Hauck, TBA-20-30) is used to produce the mainstream air flow. It is operated by a variable–frequency motor drive (Cutler Hammer, AF 95, which provides a flow rate of up to 1.42 m^3/s (≅ 3000 cfm). The blower operates in the 'suction mode' in the sense that the turbine section has been located on its suction side. The blower inlet is connected to a 292 mm (11.5") i.d. plexiglass circular duct via a diffuser with a divergence angle of 5 degress. The blower discharges air to the ambient through a 2235 mm (88.0") long, 311 mm (12.25") nominal diameter vertical pipe connected to an exhaust duct.

Measurement of Mainstream Air flow Rate

The main air flow rate is measured by a pitot tube rake (United Sensor, USNH-N-107), equipped with five pitot tubes spaced equally along a manifold which is installed in the 292 mm (11.5") i.d. plexiglass circular duct approximately 984 mm (38.75") upstream of the main blower inlet. The rake manifold is connected to a digital manometer (Validyne, PS309, range: 0-2" water gauge). The digital manometer also provides an analog output (0-2V) which is

routed to the data acquisition system (Analogic, DATA 6500). The mean and RMS values of the main air flow rate are obtained over every 1024 data points with sampling period of 0.1s.

Secondary Blower

The secondary (purge) air is supplied by another centrifugal blower (2.24 kW, Hauck, TBA-16-3) equipped with a variable-frequency motor drive (Emerson, Prism). The maximum flow rate that can be provided by the blower is 0.12 m^3/s (≅ 250 cfm). The blower discharges air through a 50.8 mm (2.0") nominal diameter insulated galvanized iron pipe to a turbine flow meter. To ensure well-developed flow upstream of the flow meter, a 760 mm (29.9") long straight pipe section has been provided upstream of the flowmeter. The secondary air then flows through a check valve to a 1524 mm (60.0") long, 19.06 mm (0.75") i.d. plexiglass tube to the center (hub) of the disk cavity. To straighten the airflow, a honeycomb section (12.7 mm (0.5") long, 3.2 mm (0.126") hexagonal cell size) has been installed in the Plexiglass secondary air tube 1600 mm (63.0") upstream of the inlet to the cavity.

Measurement of Secondary (Purge) Air flow Rate

A turbine flowmeter (EG&G Flow Technology, FT-32) measures the secondary air volumetric flow rate. The flow meter indicator provides an analog output signal that is routed to a digital multimeter (Model 45, Fluke). Via a known calibration, the voltage is then converted to air volumetric flow rate.

Rotor

The rotor disk is 25.4 mm (1.0”) thick and 403.22 mm (15.87”) in diameter. It is mounted on a 50.8 mm (2.0”) diameter mild-steel shaft which is belt-driven by a 2.24 kW (3 HP, 1750 rpm max, GE) motor. The speed of the motor is controlled through a variable-frequency drive (Dynamatic, AF1500). The speed ratio of rotor disk to the motor wheel is 3.27:1, allowing a maximum rotor speed of 5722 rpm. The rotor speed is measured by a digital photoelectric tachometer (Biddle Instruments) which uses an infrared electronic sensing system (accuracy of measurement = ± 2 rpm). While the main airflow also helps drive the rotor, the motor drive is needed for maintaining the rotor at a particular rotational speed during the experiments.

2.1 The Turbine Stage

Figures 2.1 (a) show the turbine stage schematically. The stage has been located on the suction side of the blower in order that the rotor-stator disk cavity remains optically accessible from the radial direction as well as the axial (air inlet) direction. The stage is equipped with nozzle guide vanes (59), rotor blades (52) and stator vanes (59). The stator vanes which are situated downstream of the rotor disk are 26.0 mm (0.9”) in height, and 362 mm (14.2”) in length measured from the leading edge of the vanes. The rotor blades are, 25.4 mm (1.0”) in height, and 362 mm (14.2”) in length. A 120.7 mm (4.75”) long hexagonal honeycomb section (Polypropylene, 0.315” cell size, black, Plascore, PP30-5) is provided in the annular passage 152.4 mm (6.0”) upstream of the leading edge of

the stage 1 vanes to straighten the incoming flow. It is important, however, to be mindful of the pressure drop introduced by the honeycomb section.

The stator disk which is located downstream of the rotor disk is 28.0 mm (1.10”) thick and has a diameter of 403.22 mm (15.87”). Inlet guide vanes are situated in the main gas path annulus, 26.0 mm (0.9”) in height, and 362 mm (14.2”), turn the mainstream air flow by an angle of 35 degrees applying a realistic swirl to the main airflow.

The rotor disk, of the same diameter as the stator disk, features 52 partial-height blades. The partial blade and vane heights allow the axial velocity of the main air in the annulus to be adequately high given the main blower capacity. The radial clearance between the blade tip and the plexiglass outer shroud is 1.5 mm (0.059”).

Figures 2.1 (b) shows the mid-span shapes of the vanes and blades.

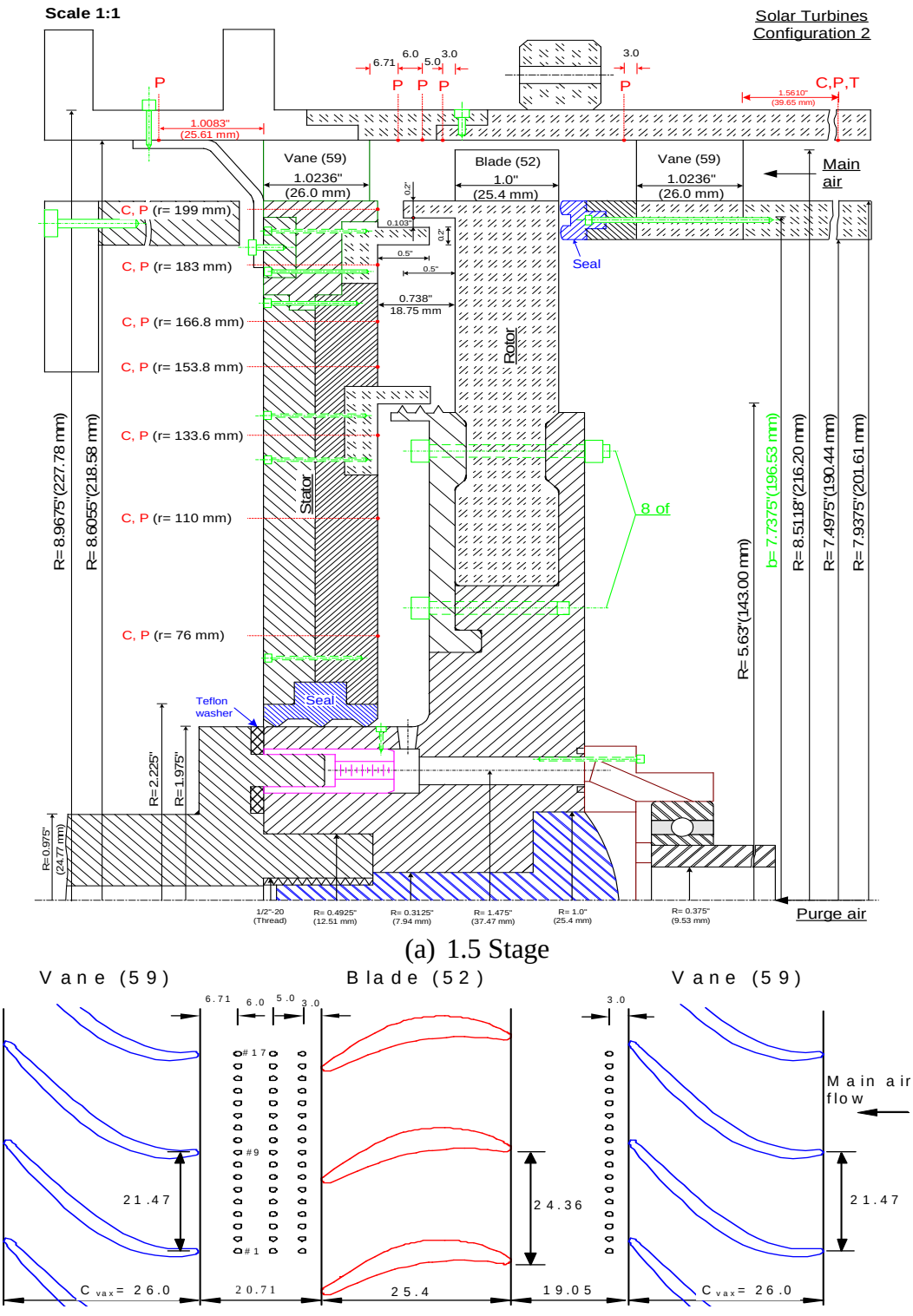

(a) 1.5 Stage

(b) Blades and Vanes

Fig. 2.1 Schematic of 1.5 stage rim seal arrangement (C: tracer gas concentration tap, P: time-avg static pressure tap); all dimensions in mm

In figure 2.2, a velocity triangle diagram for the main air flow at vane exit is shown. β_2 is the angle, with respect to the axial direction, of the main air velocity relative to the blade. β_2 must be positive for the rotor to operate in the turbine mode. It would be important to determine the velocity triangle just upstream of the blade (i.e., when the main air is about to enter the blade row). However, this would require knowledge of V_2 at that particular location. Note that V_2 will be altered somewhat as the air proceeds from the vane row to the blade row.

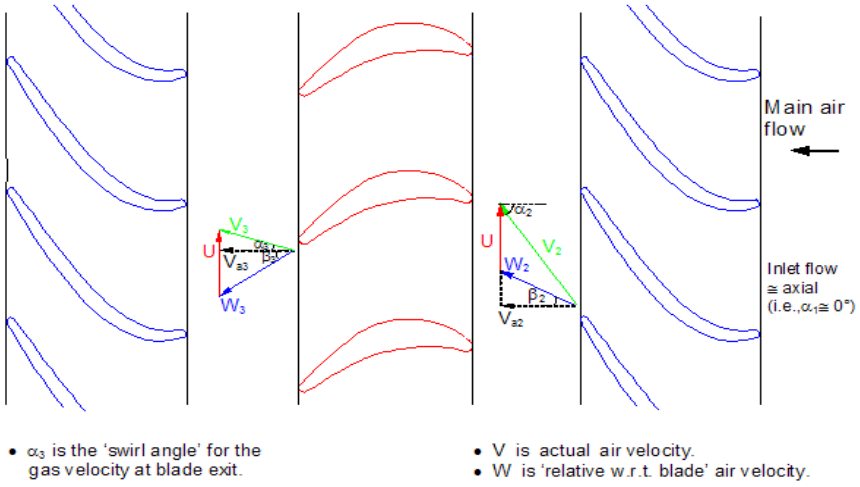

Fig. 2.2 Velocity triangle at vane exit

Purge air, which is supplied at the disk cavity hub, flows radially outward in the cavity and is eventually ejected into the main gas path through the rim seal gap. 6 equally distributed holes of diameter 2.03 mm; (as shown in fig. 2.3) are used to distribute the secondary air into the disk cavity. The maximum purge air flow rate considered in our experiments is a small fraction (~ 0.01) of the lowest mainstream air flow rate and hence not likely to effect a significant change in the

main gas path velocity triangle. The purge air is known, however, to affect the structure of the main flow.

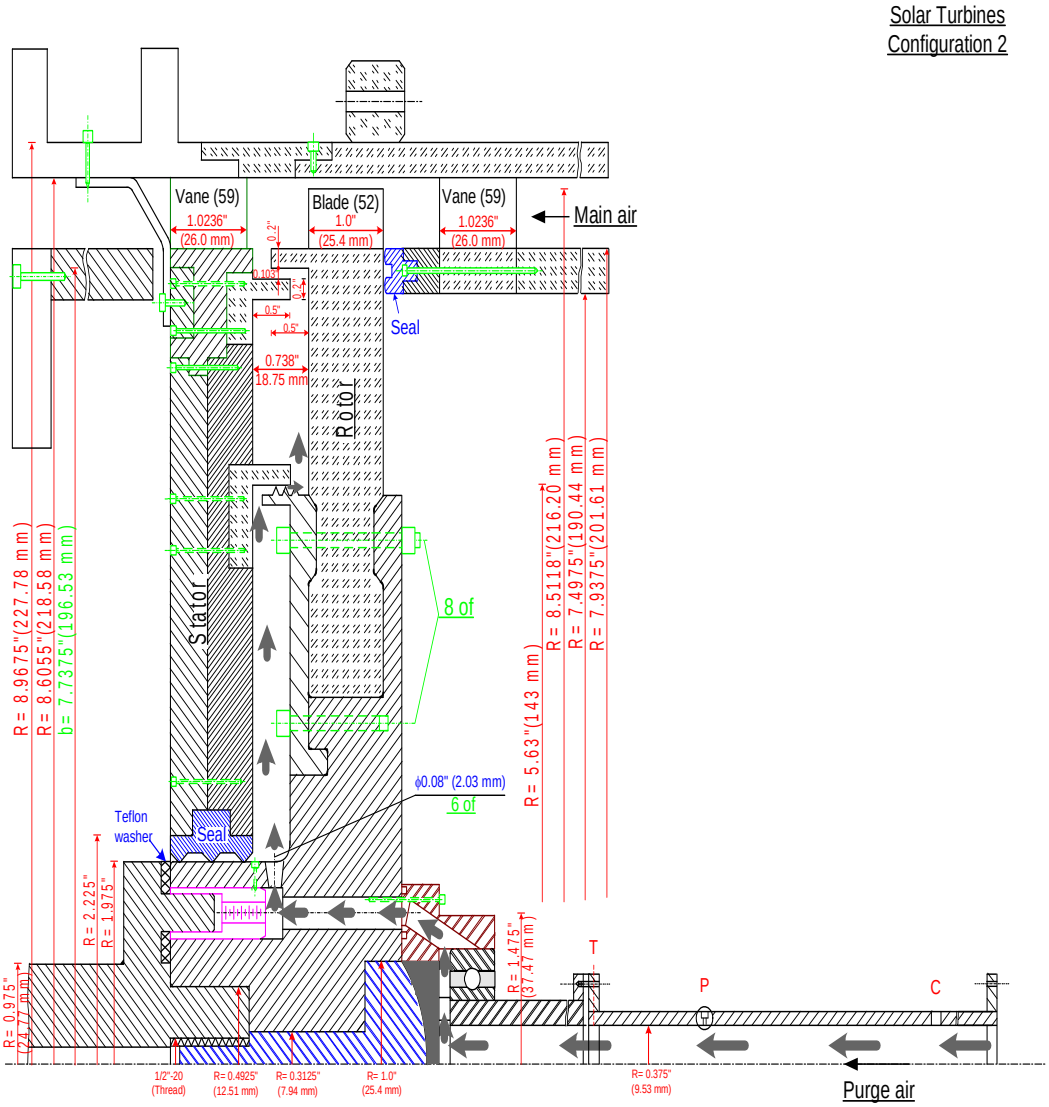

Fig. 2.3 Air flow schematic for 1.5 stage model

Rim seal configuration

Figure 2.1 (a) illustrates the single-rim seal arrangement – the stator is provided with an inner and outer rim seal, whereas the rotor disk is provided with an outer rim seal and an inner labyrinth seal. The outer seals have an overlap of 2.6 mm (0.104”) and the inner seal and the labyrinth seal have a radial clearance of 0.75

mm (0.02”) and an axial overlap of 6.6 mm (0.264”).

The cavity axial gap, s, is maintained constant at 18.75 mm (0.73”).

2.2 Time-Average Static Pressure Measurement

2.2.1 System Components

For the pressure measurement experiment, a Scanivalve, a differential pressure transducer, and a signal carrier demodulator (Figure 2.4) are very vital.

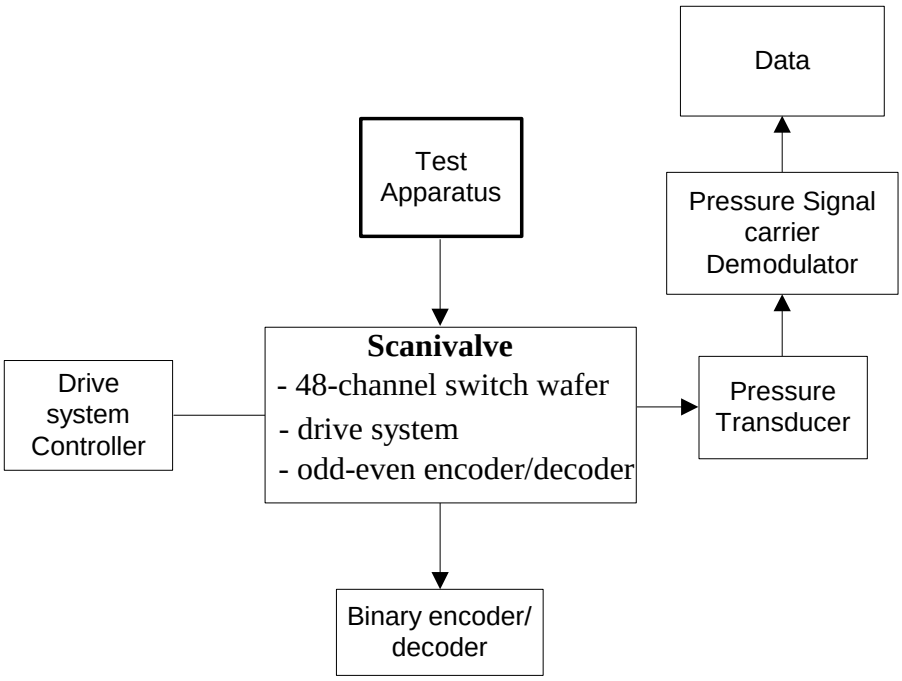

Fig. 2.4 Pressure measurement assembly

Scanivalve

The 48 inlet channel Scanivalve has one outlet channel which is routed to the pressure transducer. The 48 inlet channels are connected to the pressure taps via flexible vinyl tubes (VINL-063, Scanivalve Corp.). A solenoid step-driver rotates a fluid switch wafer so that only one of the 48 inlet channels is connected to the outlet channel at any time instant. Thus, this device allows time-

sharing one pressure transducer and its zeroing circuit among 48 different pressure inputs. A position encoder/decoder transmits the angular position of the Scanivalve, and the channel information is displayed on the scanned position unit.

Pressure Transducer

The reluctance-type pressure transducer (DP-45, Validyne) uses a sensing diaphragm to convert the pressure into electrical signal. It has a range of 0 to 2 psi (0 to 13.79 kPa). The differential pressure transducer has an open port to sense the ambient pressure and the other port connected to the output port of the Scanivalve. Elemental errors such as resolution, linearity, hysteresis, zero shift, thermal sensitivity, and drift due to environmental temperature changes determine the accuracy of the transducer.

Pressure Signal Carrier Demodulator

A Validyne CD12 pressure signal carrier demodulator is utilized as external signal conditioning module and external power supply to the DP45 pressure transducer. The circuit has a selectable gain to observe the small deviations in the signal in detail. It also has a full-scale output of 10 Vdc which can convert the output of the transducer into a high-level DC voltage signal. This analog signal is displayed on the digital LED front panel or it can be transferred to and analyzed with a data acquisition system.

Data Acquisition System

As depicted in figure 2.4, the analog signal from the pressure signal carrier demodulator is transferred to the data acquisition system via BNC cable. The data acquisition system utilized here is a Universal Waveform Analyzer (Analogic,

DATA 6500). It was programmed to provide the time-mean and RMS of the static pressure signal over sequences of 30720 data points with sampling period of 500μs (2 kHz).

Time-average static pressure tap

The 48 channel Scannivalve system is connected using miniature bulged stainless steel tabulations (TUBN-063, 1.6 mm o.d., 1.0 mm i.d., Scanivalve Corp.) Figure 2.5 shows the schematic of a typical pressure tap used in the experiments. It is essential that there are no burrs from machining or dirt/ dust in the pressure taps as that might bring some discrepancy in the pressure measurements.

Pressure tap locations for single-rim seal arrangement, figures 2.1(a), (b)

There are seven pressure tap locations situated on the stator disk. They are located at the following radial locations as shown in figure 2.1 (b): r = 76 mm, 110 mm, 133.6 mm, 153.8 mm, 166.8 mm, 183 mm and 199 mm. At r = 199 mm, 4 pressure taps are provided circumferentially over one vane pitch. To study the circumferential distribution of pressure in the main gas path, 17 pressure taps are provided on the outer shroud which are distributed over two vane pitches and three axial locations; namely x = 3mm, 8mm and 14mm from the blade trailing edge. 17 pressure taps are provided circumferentially over two vane pitch on the outer shroud which are located 3mm downstream of stage 1 vane trailing edge.

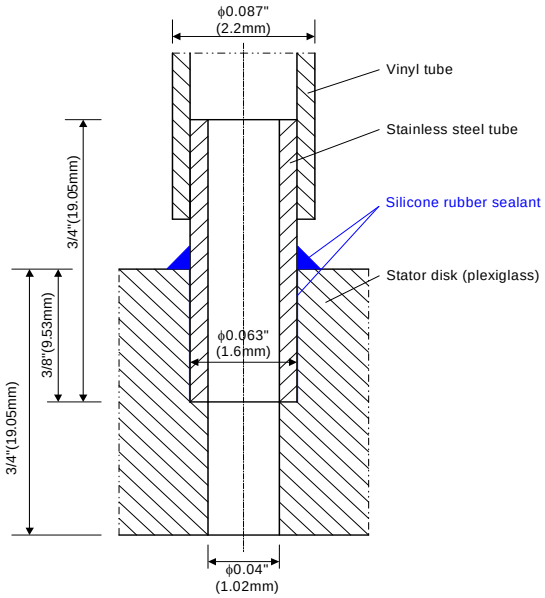

Fig. 2.5 Schematic of a static pressure tap on the stator disk

2.2.2 Experimental Procedure

To measure the main gas inlet static pressure, a pressure tap is located 40 mm upstream of the stage 1 vane leading edge. The secondary air inlet static pressure is measured at a pressure tap located 435 mm upstream of the cavity entrance. A pressure tap was introduced to measure the secondary blower discharge pressure which was located 470 mm downstream from the blower exit. Similarly a pressure tap was installed to measure the static pressure at the pitot rake which is located 950 mm upstream of the main blower entry. Along with the main inlet static pressure, the main gas outlet static pressure was also measured. The pressure tap for the main gas outlet static pressure was located 25.6 mm downstream of the 1.5 stage vane trailing edge. All these pressure reading are imperative as boundary conditions for CFD modeling and give a lot of insight into static pressure distribution throughout the entire test rig.

The time- average static pressure is defined as

$$\overline{p} = \frac{1}{T}\int_0^T p(t)dt \qquad (2.1)$$

A sufficiently large sampling rate was chosen to average out the pressure fluctuations in the readings. The lowest and highest blade frequency for our experiments 0.746 kHz (for 1780 rpm rotor speed) and 0.886 kHz (for 1900 rpm rotor speed), respectively. Accordingly, the data acquisition system was set to acquire 30720 data points at 2 kHz (500 μs sampling interval) to provide the time-average pressure. The pressure taps were sequentially connected to the differential pressure transducer. The differential pressure transducer output (a few millivolts) was amplified and demodulated by the carrier demodulator and the analog output signal (0-10V) generated was routed to the data acquisition system.

The uncertainty in the measured time-average static pressure estimated on the basis of the instrument and data acquisition uncertainties is ± 4 percent.

2.3 Main-Stream Gas Ingestion Measurement

2.3.1 System Components

NDIR Gas Analyzer

The NDIR gas analyzer (Siemens-Ultramat 23) works on the principle of; constituent gases of a sample will absorb IR radiation at a particular wavelength. Measuring the amount of IR radiation absorbed by the sample at that particular wavelength yields the concentration of the constituent gas. The gas analyzer is equipped with an IR measuring cell, a condensation trap with filter, a sample gas pump, and a flow meter. At the back of the device, two inlets – one for the sample

gas, the other for zero gas (N_2), and one gas outlet are provided. The permissible ranges for the sample gas pressure, flow, and temperature are, respectively, 0.5 to 1.5 bar absolute, 1.1 to 2 l/min, and 0 to 50^o. When switched on, the analyzer carries out a calibration (AUTOCAL) with the zero-gas (N_2). It calibrates the zero and sensitivity of the IR channel. The AUTOCAL can be manually triggered during operation by pressing the CAL key in the keypad. The Ultramat 23 can also execute an AUTOCAL cyclically; to compensate for variations in ambient temperature, pressure, and drift, a cycle time of 3 hours is selected.

One of the gases that can be traced by the NDIR analyzer is Carbon dioxide (CO_2).

Gas Cylinders and Tube Connections

A 5.0 ultra-high purity (UHP) compressed nitrogen gas is used as zero gas for AUTOCAL. A sparger tube with 15 holes; each hole being 1 mm diameter (6.3 mm o.d. and 4.5 mm i.d.) is used to seed the secondary airflow with carbon dioxide. The sparger tube is installed in the secondary air supply pipe approximately 1.7 m upstream of the disk cavity entrance. A pressure regulator (on the gas cylinder) and a needle valve (just upstream the flow meter, figure 2.6) is used to monitor the flow rate of the tracer gas and hence its volumetric concentration in the purge air. To regulate the gas as it flows from the cylinder, an electric gas heater between the gas cylinder and the regulator, and a band heater at the back of the regulator is used. The heaters also help maintain the temperature of the tracer gas (measured upstream of the valve using a J-thermocouple) close to the desired temperature.

Each of the seven concentration measurement taps is connected to seven different toggle valves by a vinyl tube (3/16” ID × 5/16” OD). These valves are connected together in the form of a manifold with a common outlet. A needle valve and a filter follow this outlet. Another vinyl tube (3/16 ID × 5/16 OD) connects the filter exit to the sample gas inlet port at the back panel of the gas analyzer.

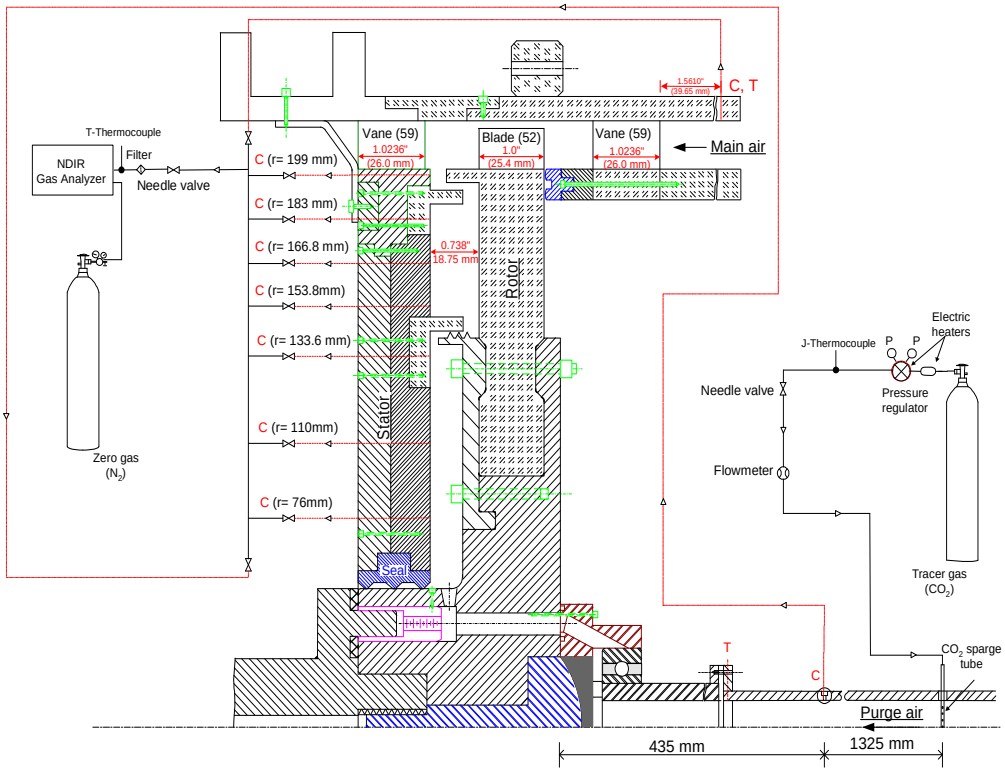

Fig. 2.6 Experimental arrangement for ingestion measurement in the disk cavity

2.3.2 Experimental Procedure

Carbon dioxide tracer gas is used for the ingestion measurement. In order to measure the concentration of CO_2 in the cavity, the purge air is seeded with tracer gas. The CO_2 volumetric concentration in the purge air is monitored just upstream (0.435 m) of its entrance to the disk cavity and maintained at 4.00 (±

0.11) percent. The pressure taps at the seven radial locations on the stator disk, Fig. 2.1(a), also serve as taps for measuring CO_2 concentration in the cavity at the stator disk surface. To measure the CO_2 concentration distribution in the cavity, sampling tubes (1 mm i.d., 1.6 mm o.d.) are installed at the same radii. The CO_2 concentration in the mainstream air is measured throughout the experiment to serve as a reference. The uncertainty in the measured CO_2 volumetric concentration is $\pm$ 0.11 percent CO_2 concentration.

Because of the nature of the technique, the ingestion measured in the cavity is rotor revolution time-averaged but local with respect to the stator vane position and the radial and axial coordinates.

2.4 Disk Cavity Velocity Field Measurement

Particle Image Velocimetry (PIV) technique is used to measure the velocity field within the cavity. PIV technique enables spatially and temporally resolved measurement of the velocity field and allows the detection of instantaneous (~ over a few μs) spatial structures in the velocity field.

2.4.1 System Components

Figure 2.7 shows a typical set-up for PIV recording. A PIV system consists of several components, each of which is described below.

Light Source

Lasers are an important component of any PIV experiment because of their ability to emit monochromatic light with high energy density. They can also be formed into thin light sheets to illuminate and record the seed particles without

chromatic aberrations.

For our experiments, a Spectra-Physics GCR-200 (dual Nd:YAG) laser is employed. Its harmonic generator converts infrared light of 1064 nm to visible green light of 532 nm by means of a KD*P crystals. The pulse width of 10 ns where each pulse has output energy of 200 mJ was obtained using a pulse repetition frequency of 10 Hz. The average power of the two lasers is 2 W. The two laser pulses must overlap and have equal power to ensure good results. Equal power in each laser pulse is ensured by measuring and then balancing with a power meter.

A Q-switch is used to shorten the pulse and raise its peak power. An optimum level of 165 μs was selected for the Q-switch delay time to produce high quality light sheet.

Light Sheet Optics

A 9 mm diameter laser was used to create a thin light sheet. To create a light sheet when using a Nd:YAG laser one has to have the right combination of the spherical and cylindrical lens. In our experiment, we used a – 50 mm focal length cylindrical lens and a 1000 mm spherical lens which produces a light sheet inside the disk cavity whose thickness varies from 70.7 μm at the waist to about 580 μm at the edge of the field of view. The lens focal lengths were calculated based on their distance from the plane of interest. Fig. 2.7 shows the combination of cylindrical and spherical lens used for our experiments. The height varies from 162 mm at the near end of the FOV to 180 mm at the far end. At the waist, the height is 171 mm. When using a light sheet for PIV experiment, one has to keep

in mind that the height of the light sheet is directly proportional to the required intensity of the laser to allow the CCD camera to capture the scattered particles. A 3-D optical traverse system was designed and implemented to allow the movement of the laser sheet in all 3 directions. The 3-D traverse system consisted of right-angled prisms (BK7), spherical, and cylindrical lens.

The lenses are mounted together on a horizontal rotary stage to deliver the light sheet parallel to the rotor. An adjustable laser arm with mirror joints directs the laser from the laser source to the light sheet optics system.

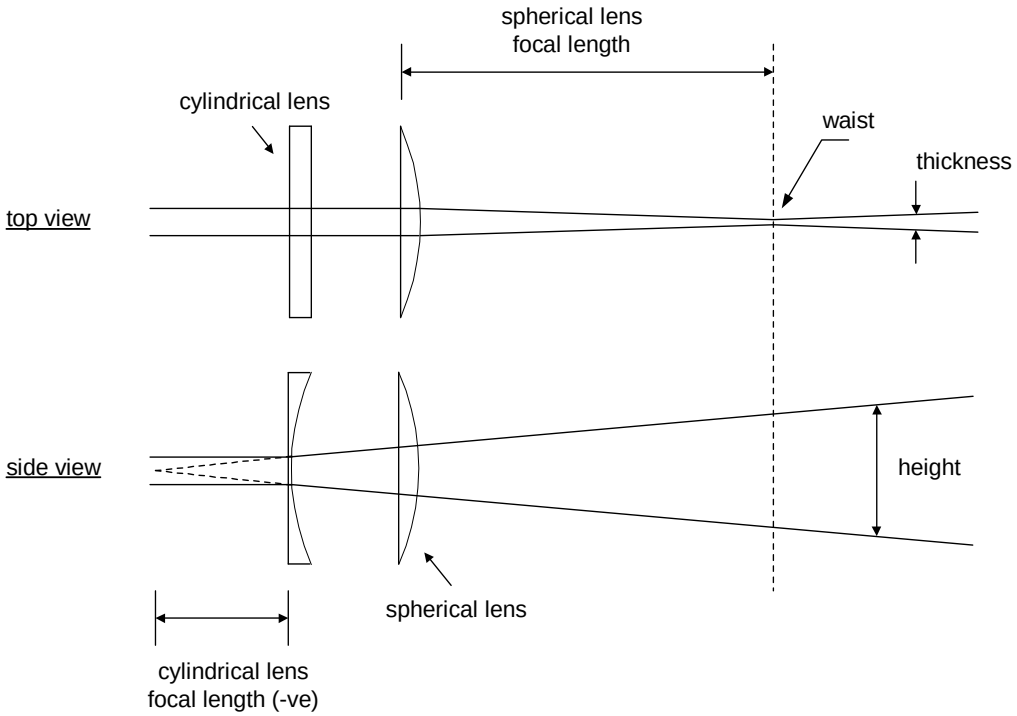

Fig. 2.7 Imaging light sheet optics

Digital Image Recording

A high-resolution CCD Cross-Correlation camera (PowerView 4M) is used to obtain the images. A CCD (charge coupled device) is an electronic sensor that converts light, i.e., photons, into charge (i.e. electrons).

A double frame/ single exposure method is used in our experiments. It provides a single illuminated image for every pulse. This method is used to give the user a general sense of particle motion and hence solving directional ambiguity. It also allows the adaptation of the pulse separation time in a wider range, and higher signal to noise ratio in the correlation plane. The CCD sensor contains 2048 x 2048 light sensitive pixels, each of 7.4 μm x 7.4 μm size.

The image capture rate is constricted by the frequency of the pulse pair provided by the laser. The maximum frame rate for our camera is 8.5 Hz and hence the maximum frame-pair rate is 4.25 Hz.

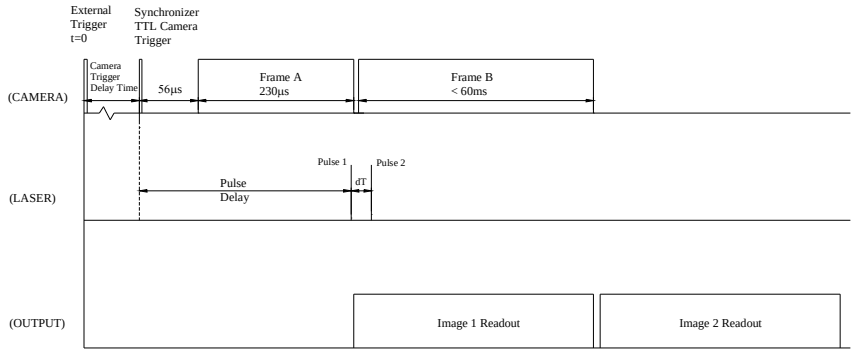

Fig 2.8 Timing diagram of Model 630150 POWERVIEW 4M camera

The maximum frequency for the Spectra Physics 200 laser is 10 Hz. The other frequencies at which the laser can operate below the maximum frequency are 5 Hz, 3.3 Hz etc. Since our camera can capture images at a frequency of 4.25 Hz or lower; 3.3 Hz was chosen to be the optimum laser frequency. Another important aspect of data acquisition is the image transfer rate and the memory storage. The frame transfer rate depends on the frame grabber which has

a transfer rate of 120 MB/s. Our laboratory computer was equipped with a 2 GB RAM. This was well within our required 52.8 MB/s (3.3 images/sec × 16 MB/image) transfer rate.

A three-dimensional traverse system allows the camera to map an entire quadrant and to move the camera towards and away from the rotor disk.

Image Synchronization

A signal generator is used to trigger the laser firing and image acquisition. The signal generator is triggered using an aluminum strip (2 x 10 mm) located on the rotor disk, aligned radially below a blade, which reflects light from a low-power laser (15 mW He-Ne laser, Melles Griot). The reflected laser is received by the signal generator through an optical fiber cable. The camera image acquisition and laser firing are controlled using software (INSIGHT 6.1) via a Synchronizer (TSI Model 610034). The synchronizer controls the imaging systems timing. The synchronizer is connects the computer, frame grabber, camera, laser and the external trigger and it conducts the time synchronization for each component as needed. The synchronizer is in turn controlled through the INSIGHT 6.1 software.

Figure 2.8 displays the timing diagram of the camera and the laser pulse. The pulse sequence begins immediately as the Synchronizer receives the external trigger. The time between the start of the pulse sequence to the time when the synchronizer triggers the camera is called as the "*camera trigger delay time*". This parameter is particularly important for our experiment since every measurement is taken at a particular rotation angle. The camera takes 56 μs to

start the first exposure after it has been triggered by the synchronizer. Similarly the first exposure is very short in duration (230 μs), which is enough to fire a Nd:YAG laser flashlamp and Q-switch. The second exposure is relatively longer (60 ms), which allows the camera to transfer the first image signal to the frame grabber before the second image can be moved to readout registry. The time from the end of one exposure to the start of the next exposure is the "*frame straddle time*". During the frame straddle time, the first image is moved via frame grabber to the computer so that the CCD array can register the second image. Another important parameter called as the "*pulse delay time*" is used to time the laser precisely towards the end of the first frame. It is defined as the amount of time from the start of the camera trigger until the first laser pulse. After the entire cycle is complete, the external trigger will wait for the next signal at the chosen blade passage and repeat the cycle to register another set of frames.

Particle Generation and Supply

Particle Image Velocimetry is an experimental technique which measures the velocity of the particle and not the fluid and hence it is important to choose the appropriate particle size and density which will disperse into the fluid and one that will have motion same as the fluid. Hence the physical properties of the particles have to be checked in order to avoid significant discrepancies between fluid and particle motion. Particle size should be select with due consideration due to the fact that PIV experiments work on the principle of scattering and hence there must be enough scattering of light from the particles for the CCD camera to register. Apart from size playing an important role in light scattering, other

properties like refractive index, shape, orientation, polarization, and observation angle have to be considered.

For our experiment, olive oil was used as seeding liquid which was atomized by means of a Laskin nozzle. Particle size usually depends on the liquid being atomized and slightly on the nozzle pressure of the Laskin nozzle. The olive oil was atomized by the Laskin nozzle (7 psig) into droplets with a mean diameter of 1.5 μm. Olive oil seed particles offer the advantage of being non-toxic, and do not change in size significantly as conditions change. Laskin nozzle has been selected for particle generation because it has been found to provide the most uniform, mono-dispersed particles compared to other particle generators.

Data Acquisition and Processing (INSIGHT 6.1)

The INSIGHT software controls all aspect of the experiment. Before any experiment, important parameters like pulse separation time (μs), pulse pair repetition time (Hz), pulse delay time (ms), Q-switch delay time (μs), camera trigger delay time (ms), and the number of image captures per trigger signal can be set using INSIGHT. The INSIGHT software is divided into two modules, an acquisition module, and a post-processing and presentation module. The first acquires the PIV image and stores it in the computer hard drive.

Obtaining a PIV vector field can be broken down into these steps: grid generation, spot masking, correlation, peak location, and validation. The input signal is broken into smaller spots by means of grid engine. Simultaneously the process manager copies the pixels into the spots and passes the spots to the spot mask engine.

The correlation engine computes the correlation function from the spots which are conditioned by the spot mask engine. The correlation function is then converted into a correlation map; the peak engine finds the peak location in the correlation map. The process manager then computes the velocity. This loop continues until all of the grid points have been processed.

The important parameters are described below.

Grid Engine

Since the images were captured in the frame straddle mode, two frames were obtained, which were later processed. Each frame was broken into smaller spots, Spot A for Frame A and Spot B for Frame B.

The Process Grid is a list of Grid Points where each Grid Point defines the pixels that make up Spot A and Spot B. A 'RecursiveNyquistGrid' was chosen as the Grid engine for our experiments. The 'RecursiveNyquistGrid' is a typical multi-pass processing grid engine, which was used during our experiments because of its accuracy and higher spatial resolution. The first processing pass computes the vector field at the 'Starting Spot Sizes' with Nyquist, 50% overlap grid spacing.

A 'Start Size Spot' and a 'Final Spot Size' of 32 × 32 pixels for both Spots A and B were found to provide a better velocity distribution with the flow conditions under investigation. As our starting and final spot sizes were the same, the second pass used the optimized window offsets to re-compute the vector field with the same number of vectors.

Maximum Displacement

The Correlation Engine uses the maximum displacement value to limit the correlation map search area to ± max displacement pixels from the zeroth pixel. This value was set to 8 for our experiments following the ¼-displacement rule of thumb.

Spot Mask Engine

The Spot Mask Engine is used to modify or condition the image spots before processing. But since the correlation engine used for our experiment was the Hart correlation which operates with non-square spots too, we did not choose any mask for the spot mask engine.

Correlation Engine

The correlation function is computed using the Correlation engine which also returns the correlation map used for processing. The correlation function is an algorithm that sums the particle image matches at all pixel displacements within the displacement range. The highest correlation map pixel is assumed to be the particle image displacement peak caused by the contributions of many particle pairs.

Hart correlation engine was used for our experiments because it reduces sub-pixel bias error and eliminated spurious vectors. Hart correlation engine uses the compression ratio to set the number of pixels that will be used to compute the correlation map. Hart correlation engine has a default compression value of 0.9, which means that 10% of the most significant pixels were used in the correlation. A high compression ratio will increase the processing speed. When the Hart

Correlation is selected, ‘BilinearPeak’ is set as the default ‘Peak Engine’.

PIV experiments can produce a very accurate (95%) velocity measurement if proper measures are taken. Several filters can be used to remove spurious vectors caused by lost pairs which can be a result of in-plane and out-of-plane motion, or low seeding density which can cause low correlation signal. The software has several built-in filters such as standard deviation, range, median, mean, double correlation, smooth, etc. By manually selecting a set of filters and settings, vector files can be validated one at a time or in a batch. The software has built-in function to interpolation and fill hole in vector fields.

2.4.2 Procedure

The experimental setup has been adapted to make quantitative velocity field measurements in the rotor-stator cavity. A three-dimensional traverse system for the camera is located approximately 80 cm from the cavity entry to avoid any disturbance in the main airflow. A second traversing system allows the light sheet generating optics to move in all the three coordinates as well.

A 50 mm lens was chosen for the camera for all our experiments since it was appropriate for the required Field of View (FOV). The image magnification factor of 0.107 (M = 1/9.28) was obtained by substituting f = 50 mm and d_o = 514.0 mm in the lens equation.

$$\frac{1}{d_o} + \frac{1}{d_i} = \frac{1}{f} \tag{2.2}$$

where d_o indicates the focused object-lens distance, d_i the image-lens distance, and f the focal length of the camera lens. Using this magnification factor

and the active area of the detector array (15.4 x 15.4), the field of view on the r-ϕ plane was computed to be 141.08 × 141.08 mm. 10 instantaneous images were taken for each set of experiment. A single ensemble- average file was generated using all 10 images. PIV experiment was carried out for four different axial locations within the cavity. The laser position was moved using the optical traverse. Experiments were done at: 5 mm, 9.7 mm, 11 mm, 14.85 mm from the stator surface. Fig. 2.9 shows the stage with the axial laser locations.

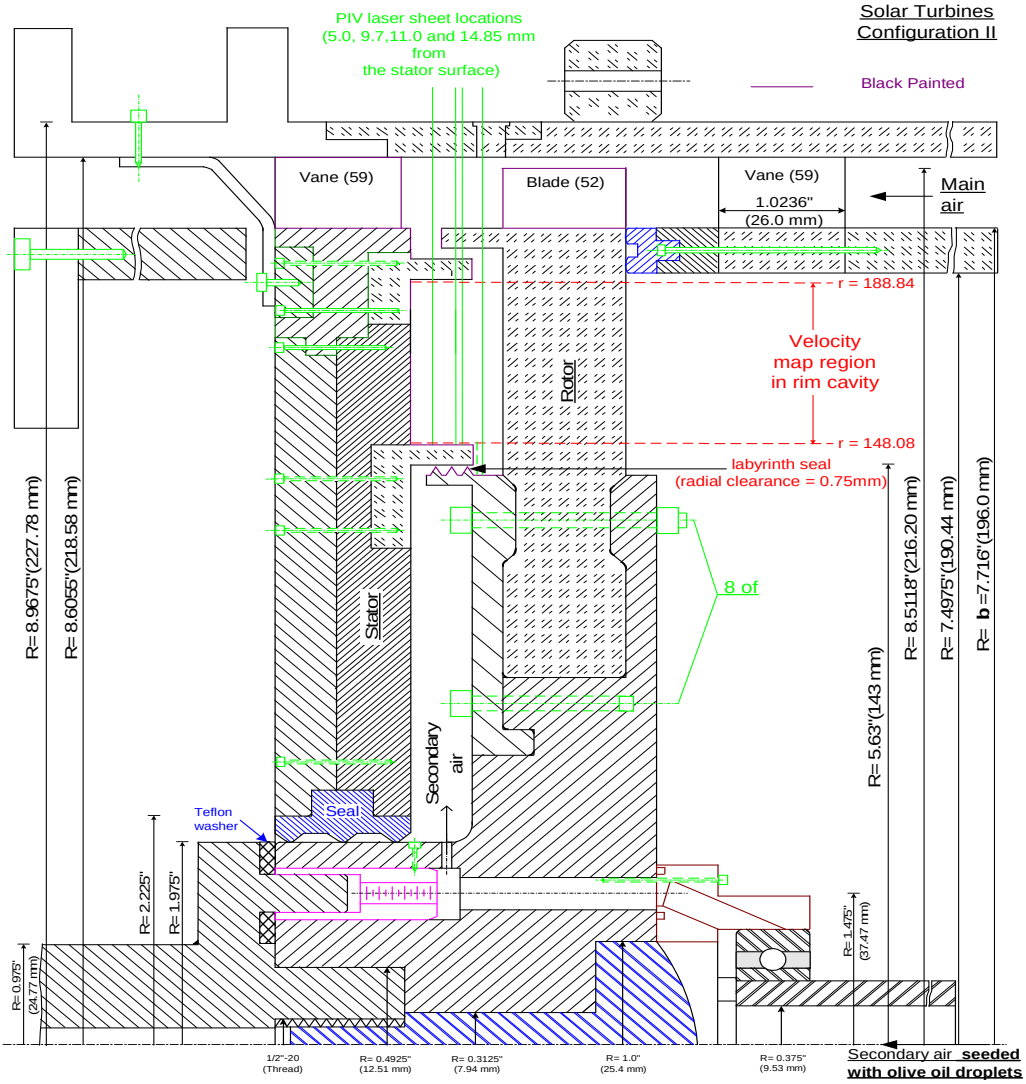

Fig. 2.9 Laser sheet with axial locations

For each location, the camera was traversed accordingly. Figure 2.10 shows the quadrant of the rotor-stator disk cavity where the PIV images of the radial(r) – azimuthal(ϕ) plane velocity field were obtained.

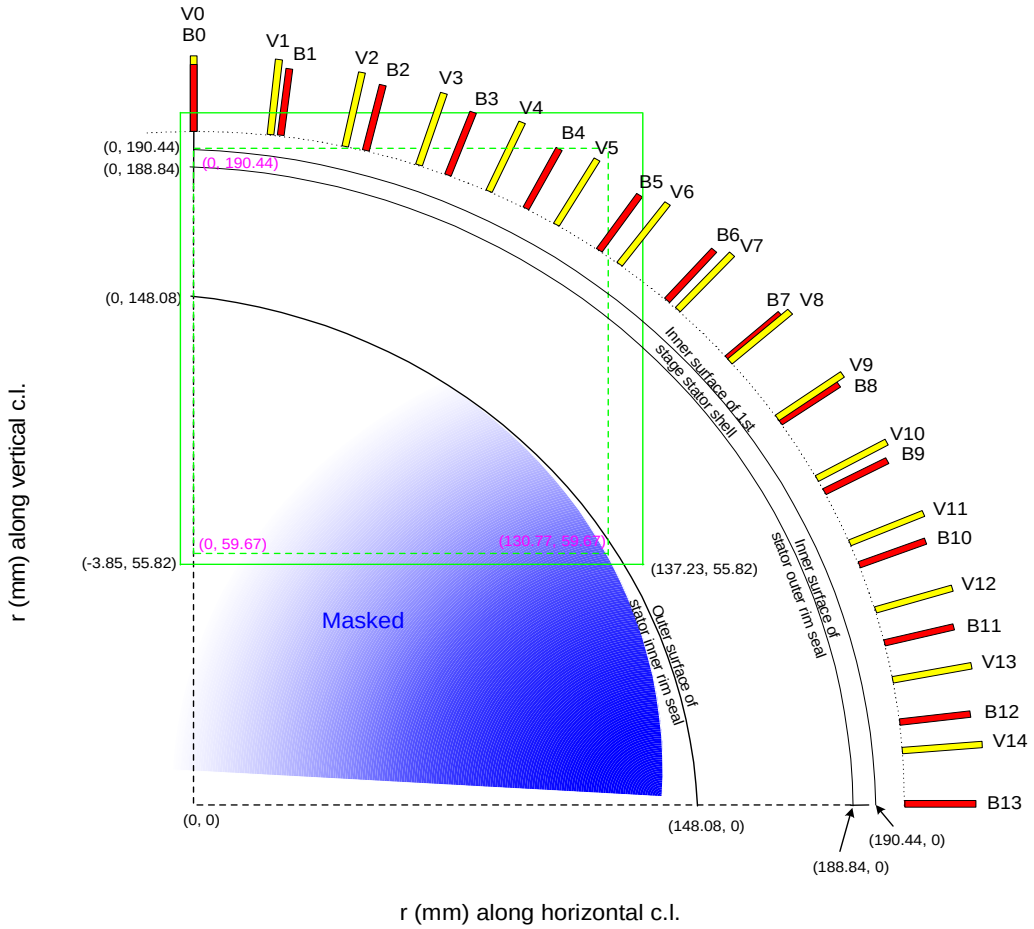

Fig. 2.10 One quadrant of a stator showing the relative vane-blade position and the coordinates of the imaging area (green). The dotted regions indicate the actual area where the velocity vectors are plotted.

At the end of an experiment, INSIGHT produces an image files with two frames which contains particles. After the image files are correlated, INSIGHT produces a vector file which contain the pixel locations and the velocities in x and y directions. These pixel coordinates are translated into the coordinates of the

experimental setup. The instantaneous as well as ensemble-averaged vector fields are then exported to MS Excel where a routine, utilizing the actual locations of the velocity vectors, splits them into radial and tangential velocities. These data files may then be plotted by TECPLOT to obtain color velocity fields.

Chapter 3

RESULTS AND DISCUSSION

3.1 Experimental Parameters and Conditions

The non-dimensional parameters in the experiments are: main air flow Reynolds number (Re_{vax}), rotational Reynolds number (Re_{ϕ}), and mass flow rate of purge air (c_w). These are given in the following table of experimental conditions. The estimated uncertainty in the values of the dimensionless parameters Re_{φ}, Re_{vax} and c_w are respectively, ± 2 percent, ± 3 percent and ± 5 percent. Pressure measurements were taken to ensure steady and circumferentially periodic flow.

Table 3.1 Experimental conditions

Exp. Set No.	**Main Flowrate (cfm / Re_{vax})**	**Rotor Speed (rpm / Re_{ϕ})**	**Sec Flowrate (cfm / c_w)**	β_2 (^{o})	**Free Disk Pumping Flowrate (cfm/ $c_{w,fd}$)**
I	**1780 /** 6.67×10^4	**1780 /** 4.93×10^5	5/822	35.0	47.73/ 7844
			10/1643		
			15/2465		
			20/3287		
II	**1900 /** 7.12×10^4	**1900 /** 5.26×10^5	5/822	35.0	50.29/ 8264
			10/1643		
			15/2465		
			20/3287		

In this Thesis, “rim cavity” refers to the region between the labyrinth seal

and the outer stator rim seal; whereas “inner cavity” refers to the region from the labyrinth seal to the hub of the rotor disk.

The choice of purge air flow rate was made with free disk pumping flow rate ($c_{w,fd}$) as a reference. The free disk pumping flow rate is the pumping flow rate due to the rotor disk rotating freely in a quiescent environment. The time-average static pressure experiments and time-average ingestion experiments were carried out for both Set I and Set II shown in the experimental conditions table above. Results section shows the static-pressure measurements for both Sets of experimental condition whereas the ingestion results section strictly talks about Set I. PIV experiments were also performed for Set I and Set II (except $c_w = 822$). For each set of experimental condition, PIV experiments were performed at four axial locations. Results from experimental condition $c_w = 1643$ and 3287 for both Set I and Set II are shown in the PIV results section.

3.2 Time-Average Static Pressure Distribution

The circumferential distribution of static pressure in the mainstream gas path is regarded as a key factor in the ingestion/egress process. The time-average static (gage) pressure distribution is measured (i) in the main gas path – at three axial positions on the outer shroud over two vane pitch, (ii) in the disk cavity – at seven radial positions on the stator disk and at four different circumferential locations on the stator disk at r = 199 mm over one vane pitch and (iii) 3 mm downstream from the stage 1 vane trailing edge on the outer shroud over two vane pitch.

Figure 3.1 presents, for Set I and c_w = 3287, the circumferential distribution of static pressure at the main air path outer shroud at 3mm downstream of the stage 1 vanes. The static pressure varies in a periodic manner following the front vane pitch with the highest pressures occurring in the mid-region of the vane wake. Figure 3.2 shows the plot for (Set I for varying c_w) the pressure distribution at the main air path outer shroud at 3mm downstream of stage 1 vanes. Though the effect of increasing purge air flow rate on the pressure distribution on the outer shroud at 3mm downstream of stage 1 vanes is not

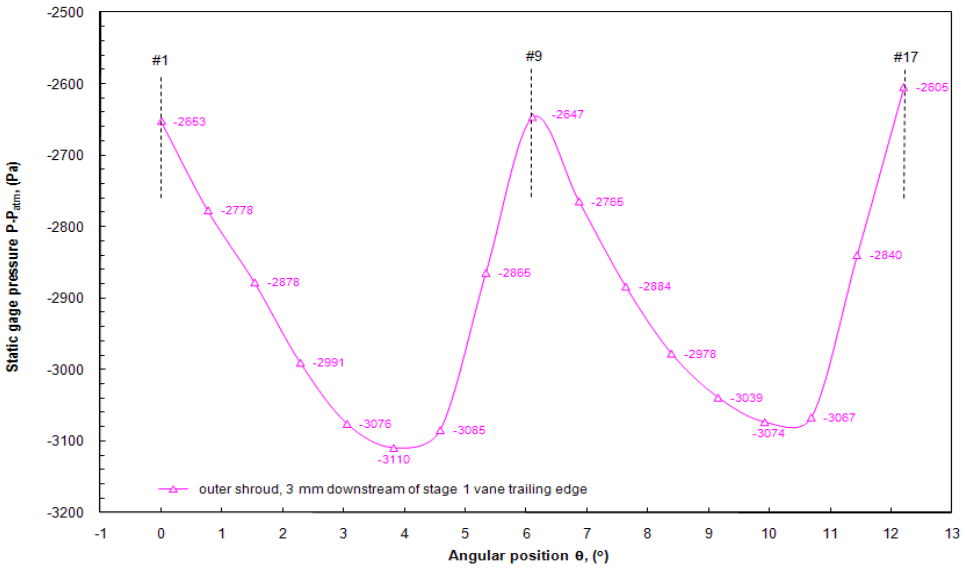

Fig. 3.1 Time-average static pressure data at the outer shroud, 3 mm downstream of stage 1 vane trailing edge for $Re_\phi = 4.93\times10^5$, $Re_{vax} = 6.67\times10^4$, c_w = 3287

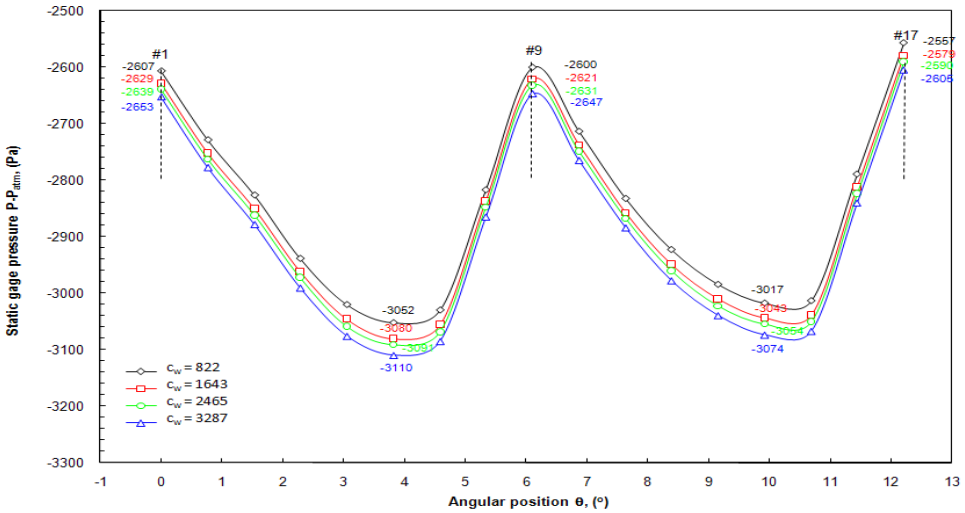

Fig. 3.2 Comparison of time-average static pressure data at the outer shroud, 3 mm downstream of stage 1 vane trailing edge for $Re_\phi = 4.93\times10^5$, $Re_{vax} = 6.67\times10^4$

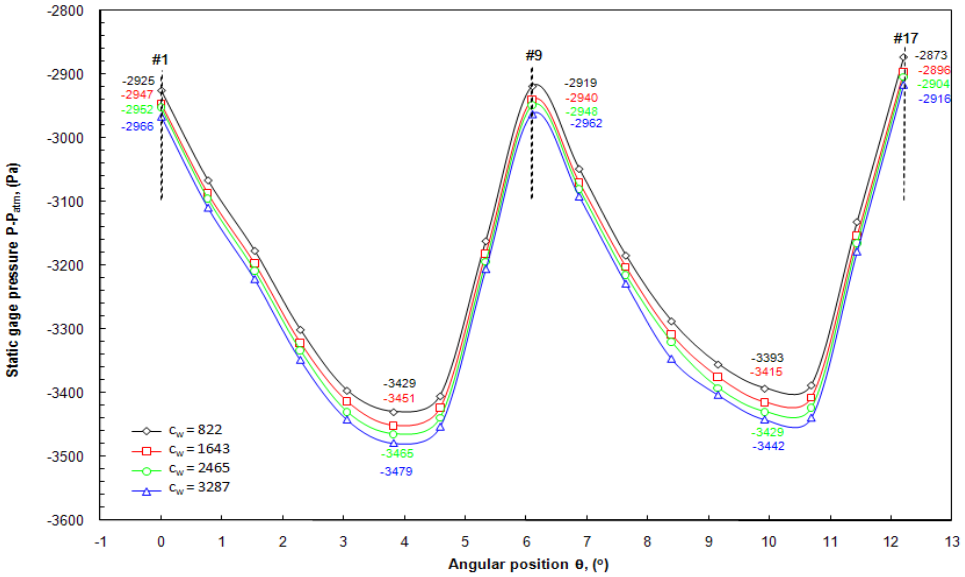

Fig. 3.3 Comparison of time-average static pressure data at the outer shroud, 3 mm downstream of stage 1 vane trailing edge for $Re_\phi = 5.26\times10^5$, $Re_{vax} = 7.12\times10^4$

significant, the pressure level reduces slightly for increasing purge air flow rates. This could be due to the entry of low pressure purge gas from rim cavity into the main gas oath. Comparing figure 3.2 to figure 3.3 (Set II), it can be said that increasing main gas flow rate and rotor speed, reduces the pressure level on the outer shroud at 3mm downstream of stage 1 vanes on an average by 350 Pa.

Figure 3.4 represents the circumferential distribution of pressure on the outer shroud downstream of rotor blades at three different axial locations and at r = 199mm of the aft cavity stator. It can be seen that the circumferential pressure distribution is periodic following the vane pitch (both front and aft); they also shift in phase in the stream-wise direction. It was noticed that, as we travel axially, the peak of the pressure distribution moves towards the aft vane leading edges. The strength of the circumferential asymmetry in pressure decreases from the 3mm axial location to the 8mm location. It, however, increases at the 14mm location possibly because of the purge air mixing with the mainstream gas in the region and mainly because of the proximity of the aft vanes. Figure 3.4 shows that increasing the purge air flow rate reduces the pressure level on the outer shroud, downstream of rotor blades. Increasing main air flow rate and rotor speed also reduces the pressure level by approximately 400 Pa. The circumferential variation of static pressure at r = 199 mm, (which is at the axial gap between the rotor rim seal and stator) is very low.

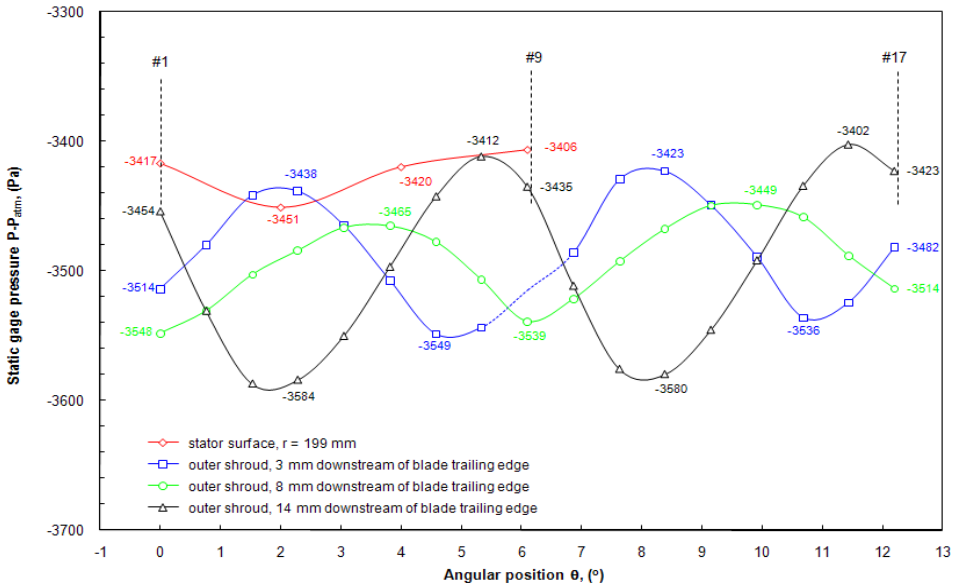

Fig. 3.4 Time-average static pressure data at the outer shroud and the stator surface near the rim seal for $Re_\phi = 4.93\times10^5$, $Re_{vax} = 6.67\times10^4$, $c_w = 3287$

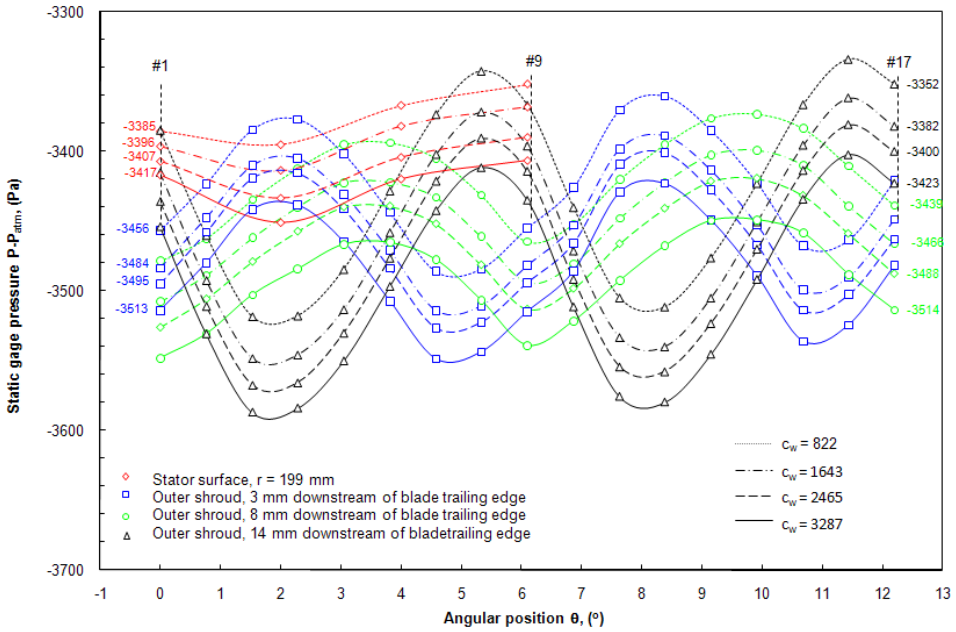

Fig. 3.5 Comparison of time-average static pressure data at the outer shroud and the stator surface near the rim seal for $Re_\phi = 4.93\times10^5$, $Re_{vax} = 6.67\times10^4$

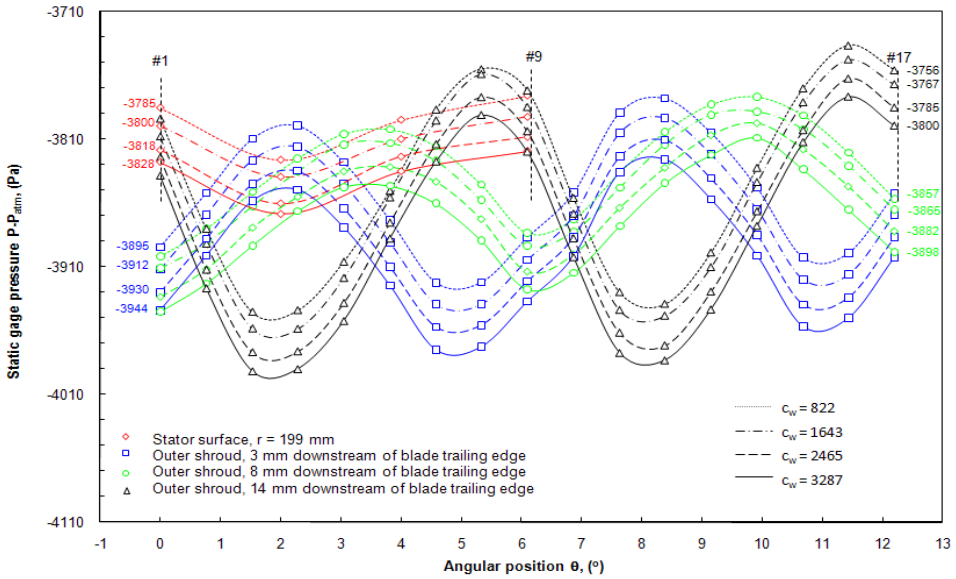

Fig. 3.6 Comparison of time-average static pressure data at the outer shroud and the stator surface near the rim seal for $Re_{\phi}= 5.26\times10^{5}$, $Re_{vax}= 7.12\times10^{4}$

Figure 3.7 and 3.8 show the pressure distribution on the outer shroud at seven different locations. The pressure in the inner cavity and the rim cavity was found to increase radially. This is mainly due to the effect of centrifugal force induced by the rotor where the fluid tangential velocity increases with the rotor disk speed which increases the pressure gradient according to the radial momentum equation. The pressure on the stator surface reduces by a significant amount across the labyrinth seal, which is caused due to the presence of labyrinth seal which has a radial clearance of 0.75 mm and hence induces a jet like flow to the purge gas. The pressure level also reduces across the stator outer rim seal which could be caused due to the interaction of low pressure purge gas and high pressure main gas. The pressure drop across the labyrinth seal was found to increase with increasing purge air flow rate.

Increasing mainstream air flow rate and rotor speed increases the peak-to-peak pressure value in the main air path which could influence ingestion of mainstream gas into the disk cavity.

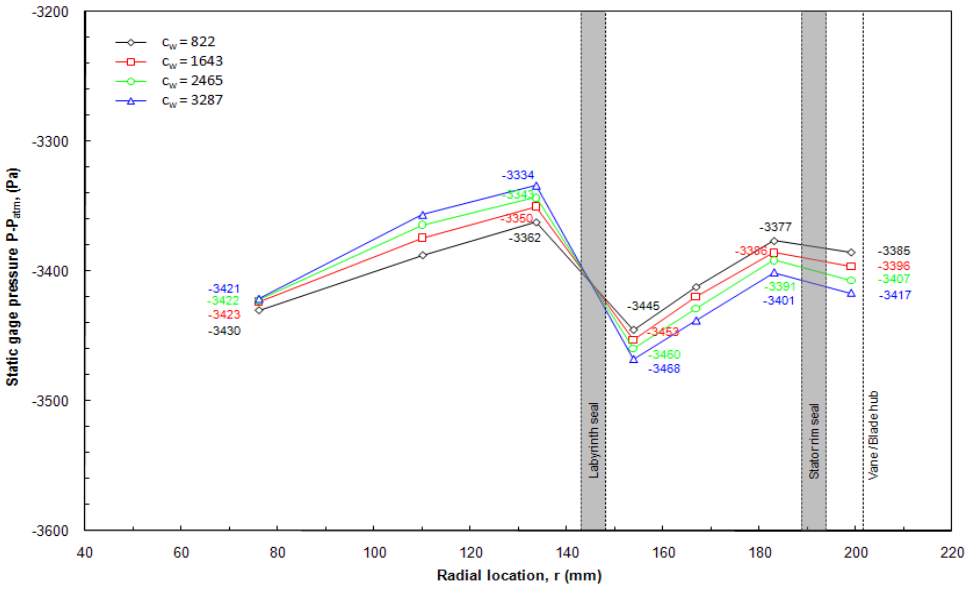

Fig. 3.7 Comparison of time-average static pressure data at the stator surface for $Re_{\phi}= 4.93\times10^{5}$, $Re_{vax}= 6.67\times10^{4}$

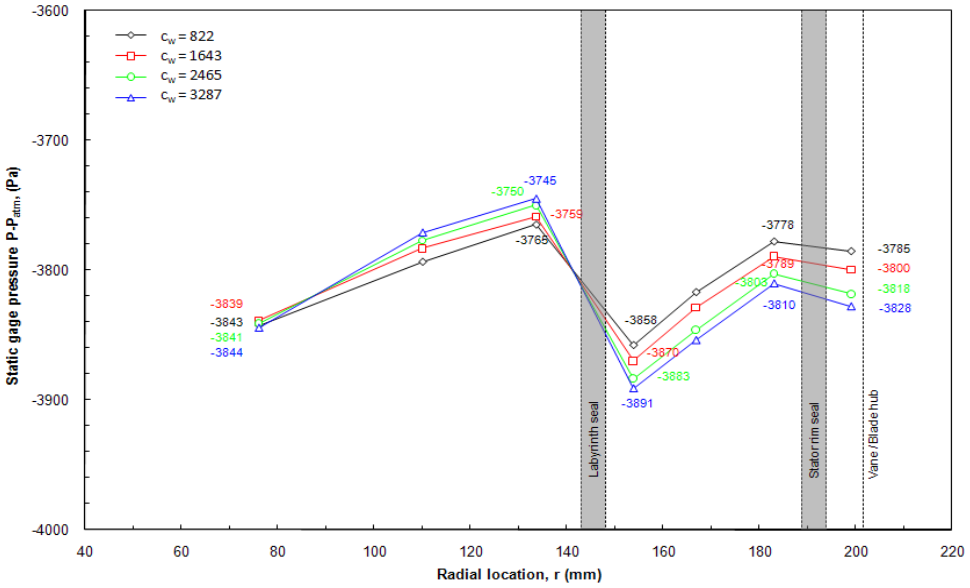

Fig 3.8 Comparison of time-average static pressure data at the stator surface for $Re_{\phi}= 5.26\times10^{5}$, $Re_{vax}= 7.12\times10^{4}$

3.3 Mainstream Gas Ingestion Distribution

This sections deals with the significance of rim seals and purge air and how they combine to reduce the effect of main gas ingestion into the rotor-stator cavity. All ingestion distributions are presented in terms of *sealing effectiveness*.

It is defined in terms of tracer gas concentration as:

$$\eta(\underline{r}) = \frac{C(\underline{r}) - C_{main}}{C_{purge} - C_{main}} \qquad (1)$$

The value of η ranges from 0 (no sealing) to 1.0 (perfect sealing).

Fig. 3.9 show the radial distribution of sealing effectiveness at the stator surface for experimental condition $Re_{\phi}= 4.93\times10^{5}$, $Re_{vax}= 6.67\times10^{4}$. It can be noted that for higher c_w, the inner cavity is effectively sealed off from mainstream gas ingestion. A major drop in sealing effectiveness is observed across the labyrinth seal for all purge air flow rates and significant ingestion into the rim cavity takes place. The purge air exits the labyrinth seal in the form of a jet which impedes the rim cavity fluid from entering the inner cavity i.e. the ingested mainstream air is predominantly restricted in the rim cavity before getting ejected out into the mainstream gas path.

At lower purge air flow rates, there was ingestion of mainstream gas into the inner cavity which means, the curtain of fluid formed by the jet is apparently inadequate to seal the inner cavity.

Ingestion measurements were also made circumferentially on the stator surface at four locations at r = 199 mm where the ingestion was found to be

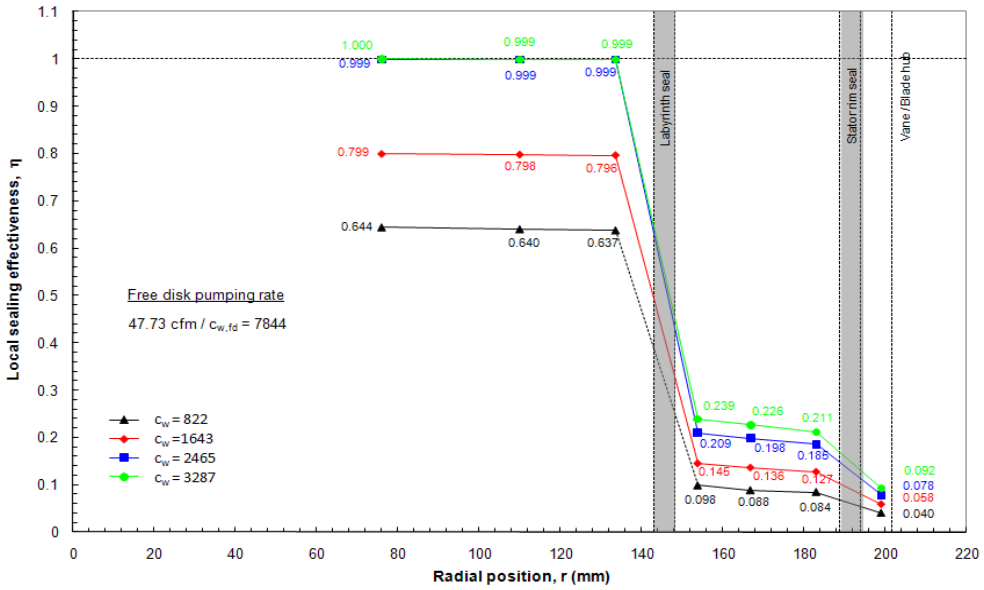

Fig. 3.9: Local sealing effectiveness on the stator surface at different secondary flow rates for $Re_\phi = 4.93\times10^5$, $Re_{vax} = 6.67\times10^4$

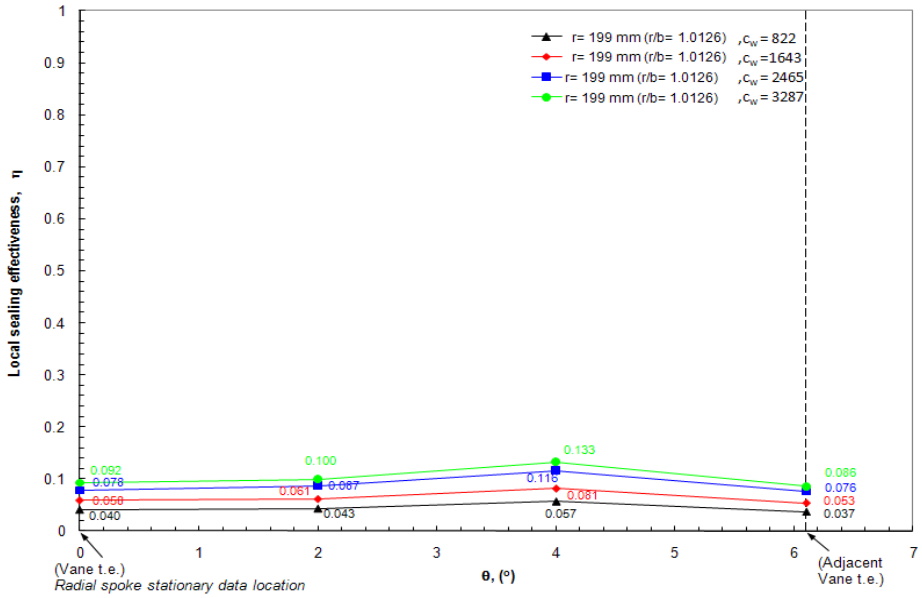

Fig. 3.10 Circumferential variation of local sealing effectiveness on the stator surface (one vane pitch) for $Re_\phi = 4.93\times10^5$, $Re_{vax} = 6.67\times10^4$

maximum. The measurements were done over one vane pitch. Fig. 3.10 shows the effect of purge gas flow on ingestion. It can be observed in the plot; the sealing effectiveness is almost uniform and hence it can be said that ingestion does not vary circumferentially. The plots also reemphasize the fact that sealing effectiveness is higher for higher purge airflow rates.

3.4 Velocity Field in the Disk Cavity

Instantaneous and ensemble-averaged velocity field are presented in this section to understand the flow field within the cavity and to study the influences of main gas ingestion into the disk cavity. At each experimental condition, the velocity vector maps were obtained at four axial positions, namely 5.0mm and 9.7 mm from the stator surface and 7.75mm and 3.9mm from the rotor surface. Ten instantaneous vector maps were obtained at each axial location.

Figure 3.11 and figure 3.12 show the velocity map for Set I, c_w = 1643 at x/s = 0.266 and x/s = 0.792 respectively. From the velocity map it can be noted that the velocity of the fluid near the rotor is higher than that near the stator. Comparing figure 3.13 and figure 3.14 (Set I, c_w = 3287 at x/s = 0.266 and x/s =

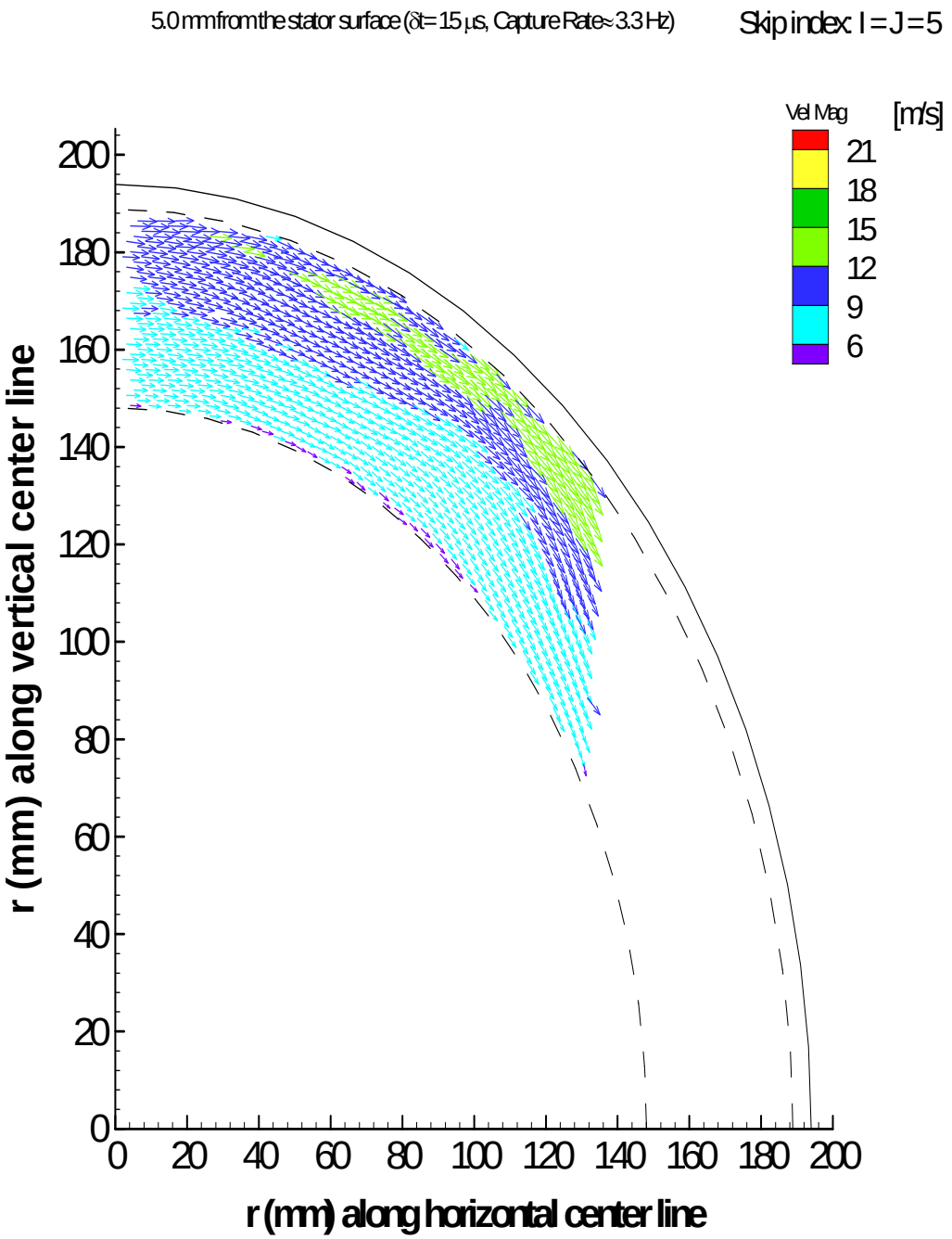

Fig. 3.11 Ensemble averaged vector map for x/s = 0.266, $Re_{vax} = 6.67\times10^4$, $Re_{\Phi} = 4.93\times10^5$ and $C_w = 1643$

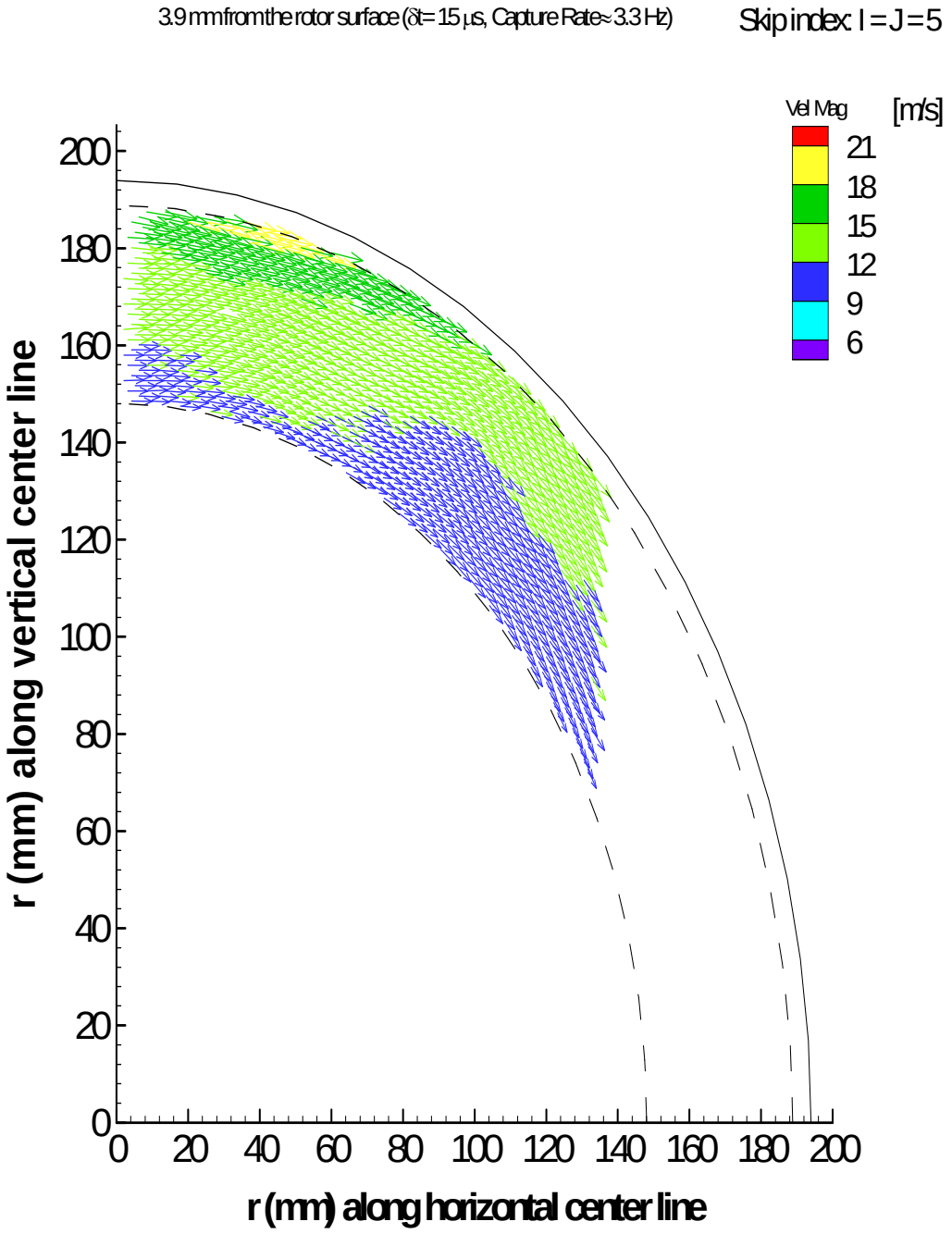

Fig. 3.12 Ensemble averaged vector map for x/s = 0.792, $Re_{vax} = 6.67\times10^4$, $Re_{\Phi} = 4.93\times10^5$ and $C_w = 1643$

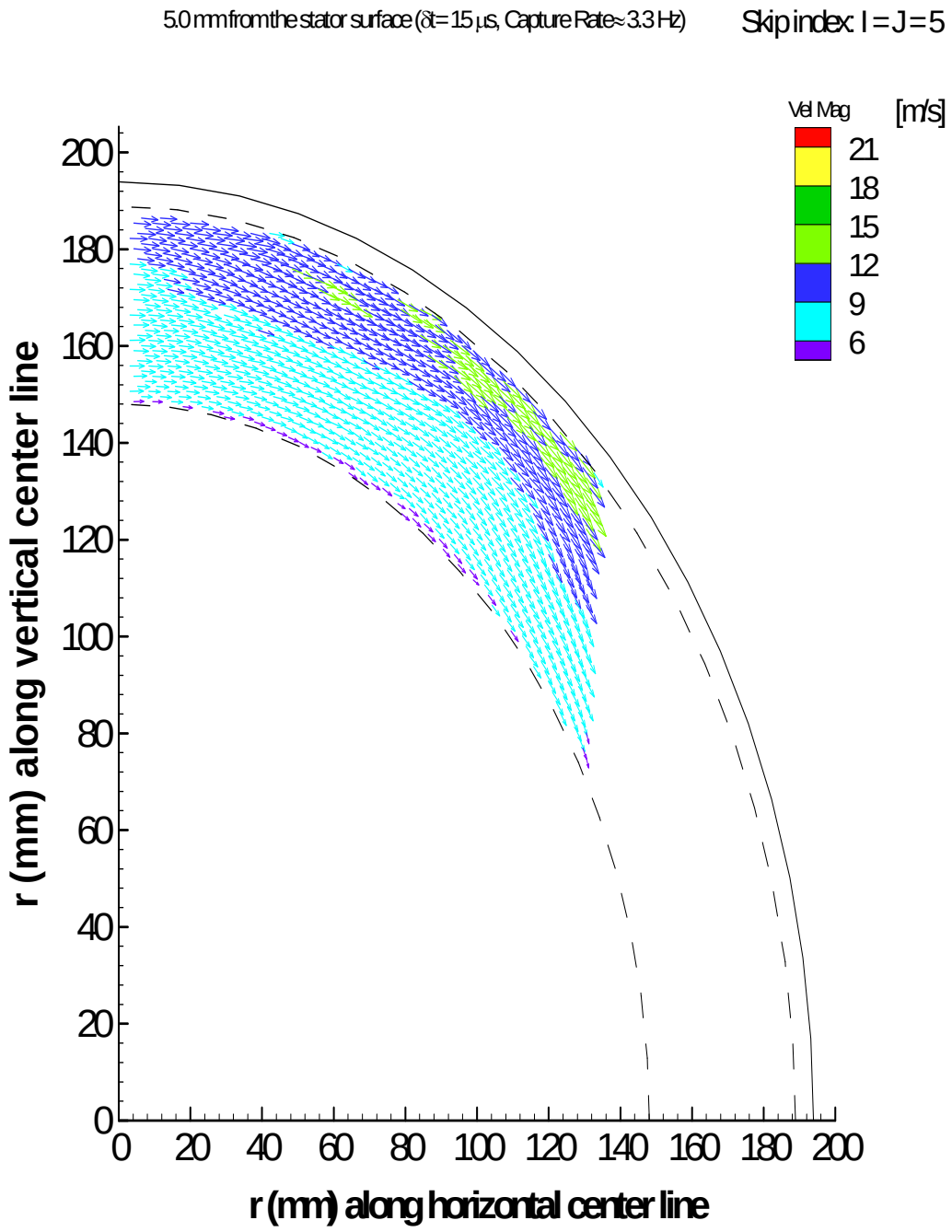

Fig. 3.13 Ensemble averaged vector file for x/s = 0.266, $Re_{vax} = 6.67\times10^4$, $Re_{\Phi} = 4.93\times10^5$ and $C_w = 3287$

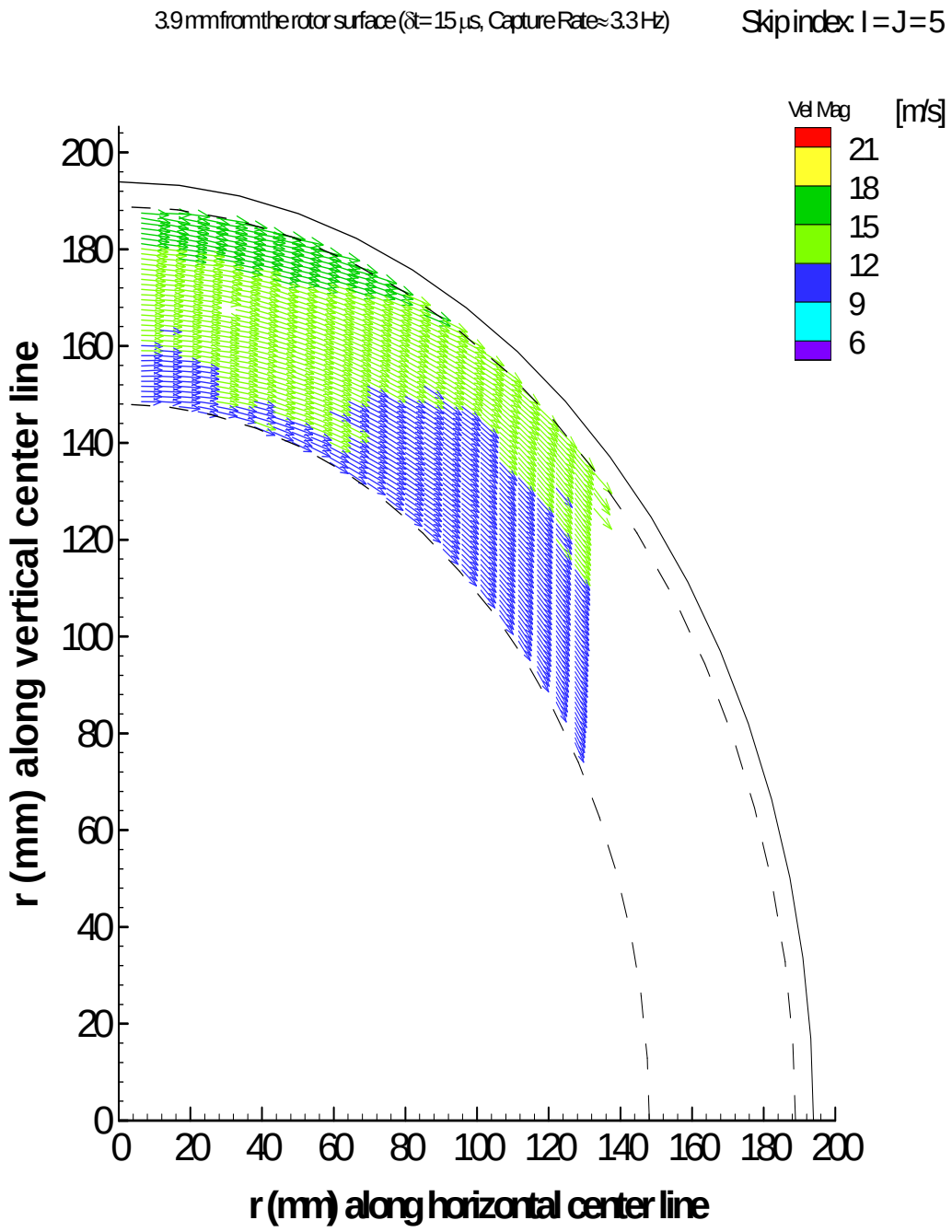

Fig. 3.14 Ensemble averaged vector file for x/s = 0.792, $Re_{vax} = 6.67\times10^4$, $Re_{\Phi} = 4.93\times10^5$ and $C_w = 3287$

0.792 respectively) to the velocity maps for Set I, c_w = 1643, the difference in fluid velocity is not significant. Increasing rotor speed and mainstream gas flow

rate however has a major influence on the fluid velocity in the aft disk cavity. Figures 3.15 and 3.16 show the fluid velocity map for Set II, c_w = 3287 at x/s = 0.266 and x/s = 0.792 respectively. The fluid velocity increases throughout the rim cavity when the mainstream air flow rate and rotor speed are increased. However for all conditions, the fluid velocity is higher near the rotor than at the stator possibly due to the disk pumping effect and because of the purge air flow into the rim cavity.

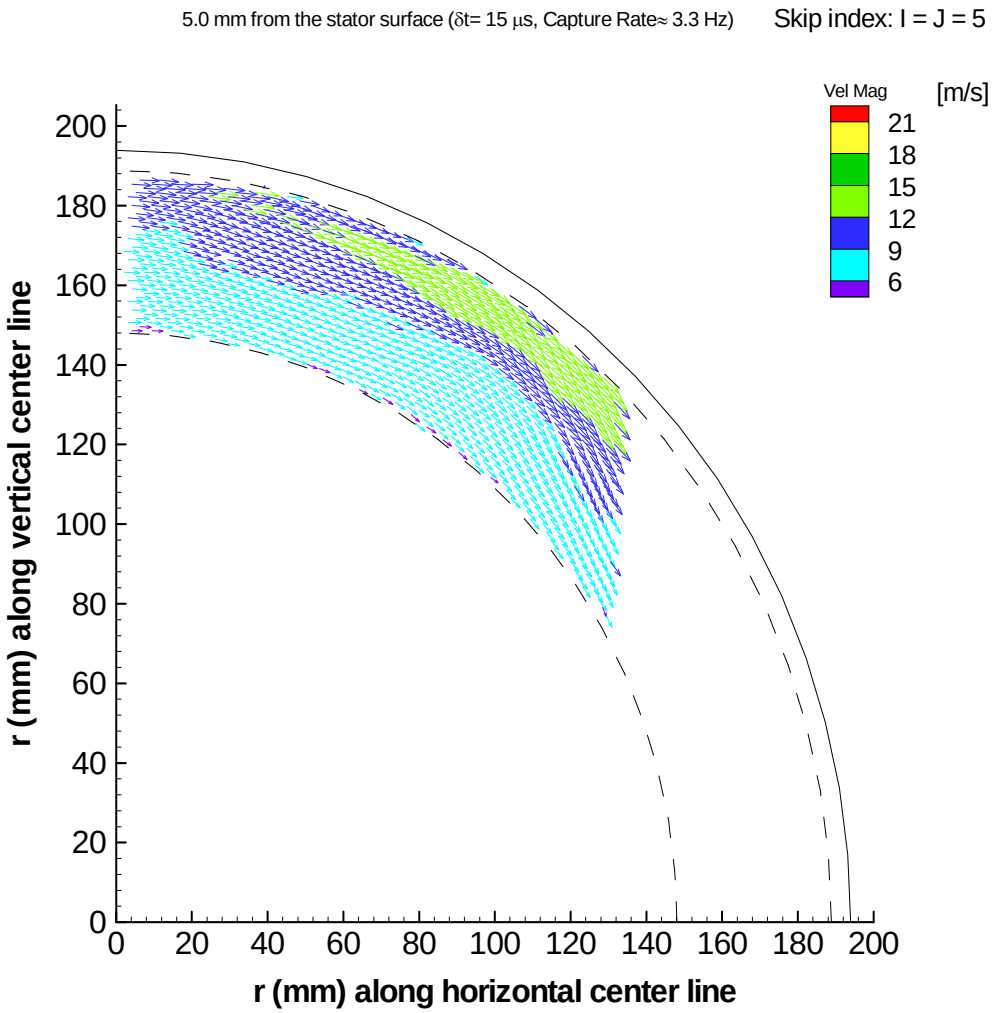

Fig. 3.15 Ensemble averaged vector file for x/s = 0.266, $Re_{vax} = 7.12\times10^4$, $Re_\Phi = 5.26\times10^5$ and $C_w = 3287$

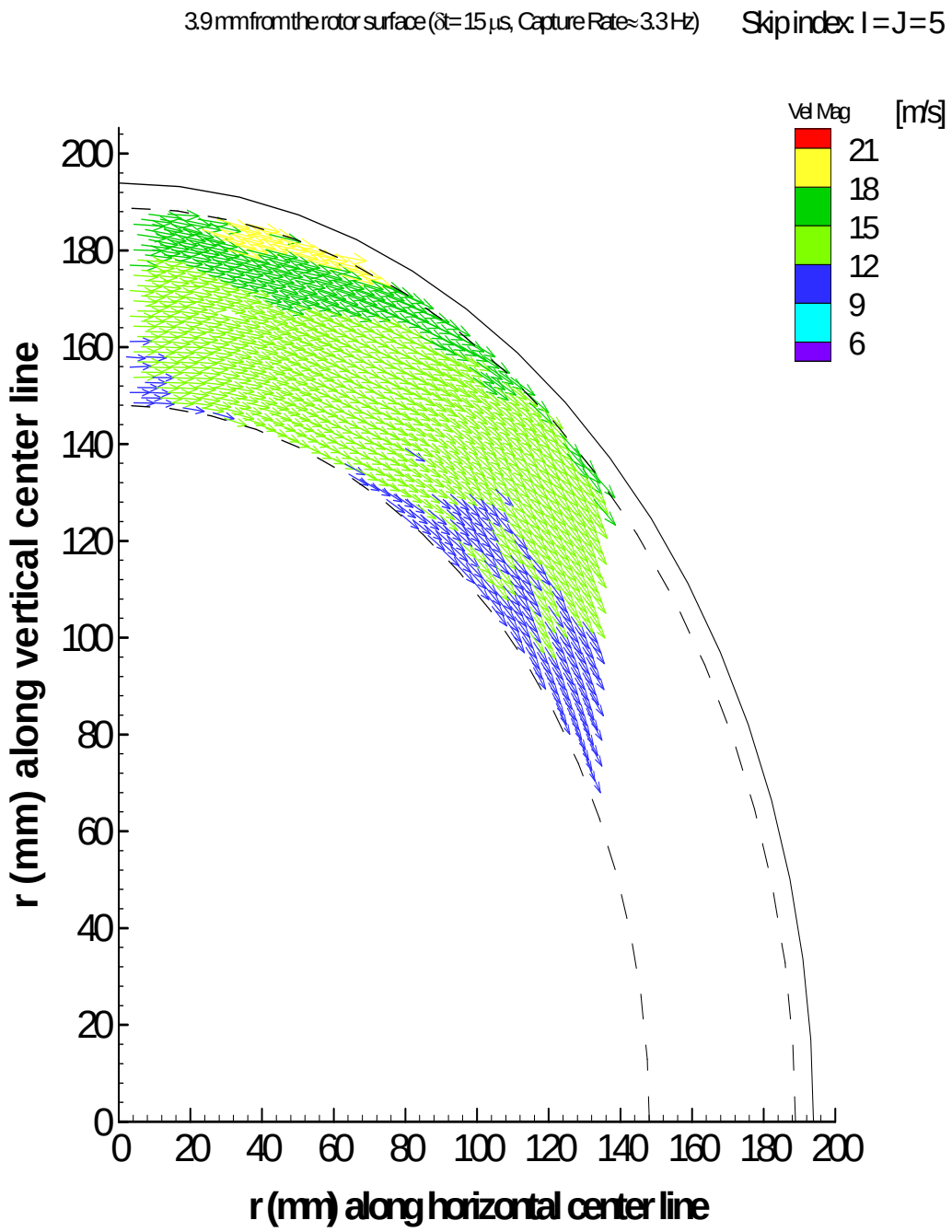

Fig. 3.16 Ensemble averaged vector file for x/s = 0.792, $Re_{vax} = 7.12\times10^4$, $Re_{\Phi} = 5.26\times10^5$ and $c_w = 3287$

Non-dimensionalized circumferential-average fluid tangential velocity $V_\varphi(r)/U(r)$ and radial velocity $V_r(r)/U(r)$ determined from the velocity map (Fig. 3.16) are show in figure 3.17 and 3.18 respectively. Tangential velocity was noted to be highest at the location nearest to the rotor and lowest at the location near the stator. It was also observed that the tangential velocity remained constant over 70% of the radial extent of the rim cavity. The dotted purple line (for 3.9 mm from rotor surface) represents the interpolated tangential velocity. It is the only location which passes the stator outer rim seal and attains the rotor velocity. For the other three locations (dotted line only shown for 5 mm (red) from stator surface), the tangential velocity goes to 0 due to the stationary stator outer rim seal. On the other hand the fluid radial velocity was very low in the rim cavity except near the rotor. This could be due to the fact that fluid velocity is primarily tangential in the 'core cavity' region. From figure 3.18 it was also noted that radial velocity was directed outwards near the rotor, which could also be because of the combined effect of disk pumping and purge air flow. At other axial locations, the radial velocity was mostly directed radially inwards; which could be because of re-circulating cavity fluid and the inward flow of ingested main air.

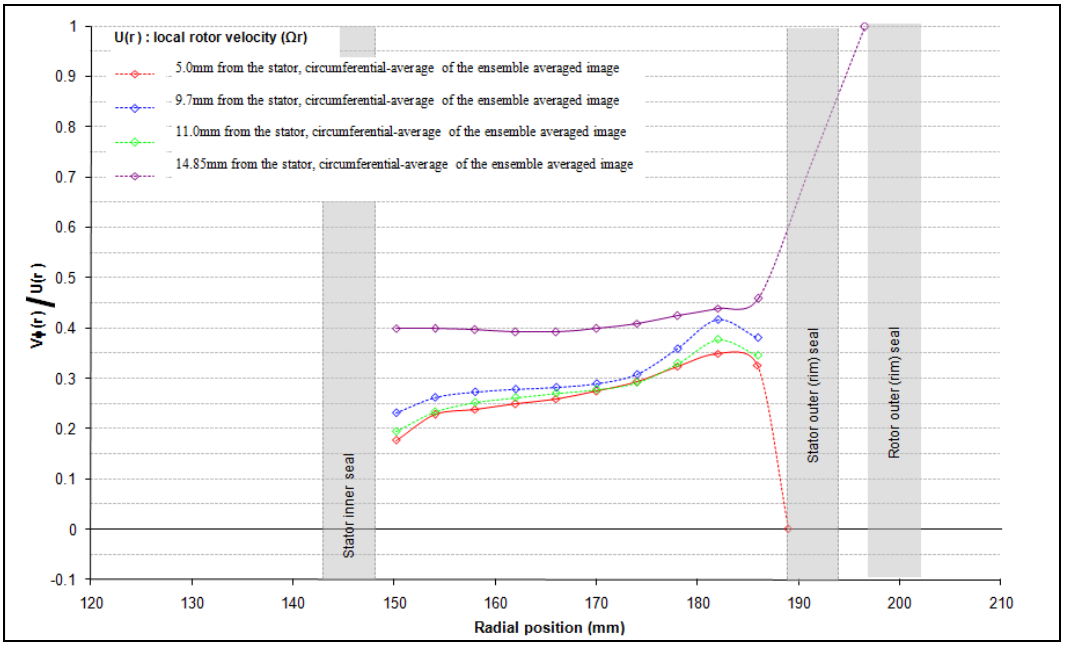

Fig. 3.17 Circumferential–average tangential velocity from ensemble-averaged maps at the four axial locations in the rim cavity for $Re_{vax} = 7.12\times10^4$, $Re_\Phi=5.26\times10^5$, $c_w = 3287$

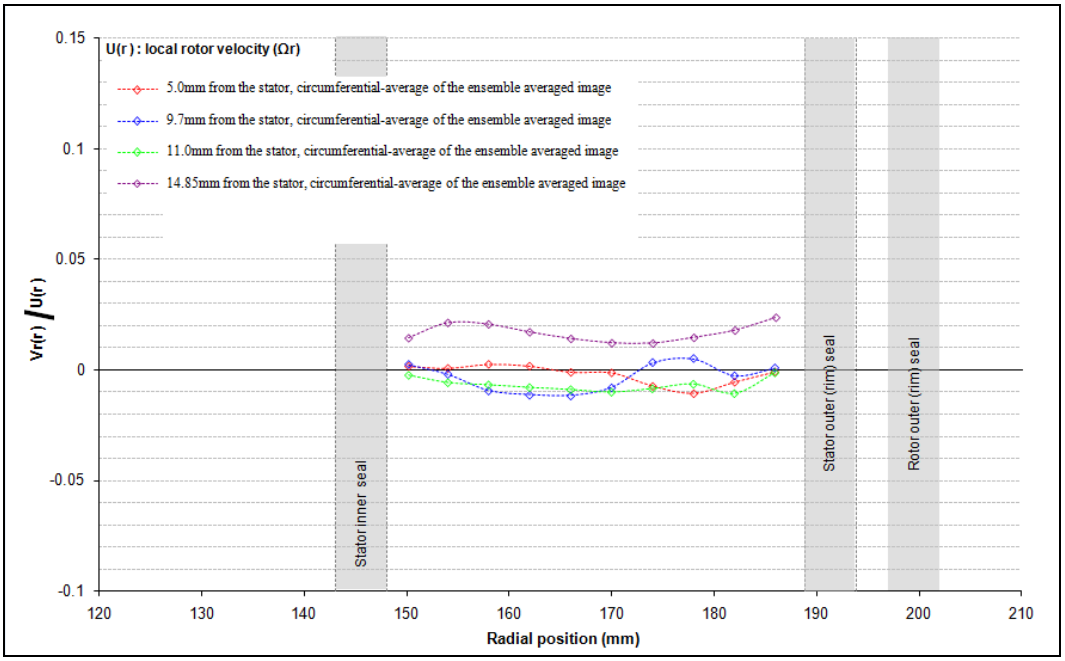

Fig. 3.18 Circumferential–average radial velocity from ensemble-averaged maps at the four axial locations in the rim cavity for $Re_{vax} = 7.12\times10^4$, $Re_\Phi= 5.26\times10^5$, $c_w = 3287$

Figures 3.20 and 3.21 show, respectively, the non-dimensionalized fluid tangential and radial velocities over two degree sectors, obtained from an instantaneous velocity vector map for experimental Set II, c_w = 2465 at 3.9mm from the rotor surface (figure 3.19). Instantaneous velocity maps are considered to preserve most of the physics behind the flow since the velocities are not smeared like in the ensemble-averaged plots. There was a large fluctuation in the fluid instantaneous radial velocity when compared to circumferential averaged radial velocity shown in figure 3.18. Regions where radial velocity is predominantly positive (i.e. fluid flowing radially inwards) and negative (i.e. fluid flowing radially outwards) were found. Tangential velocity plot also has a lot of fluctuations but is not visible due to the scale of the plot.

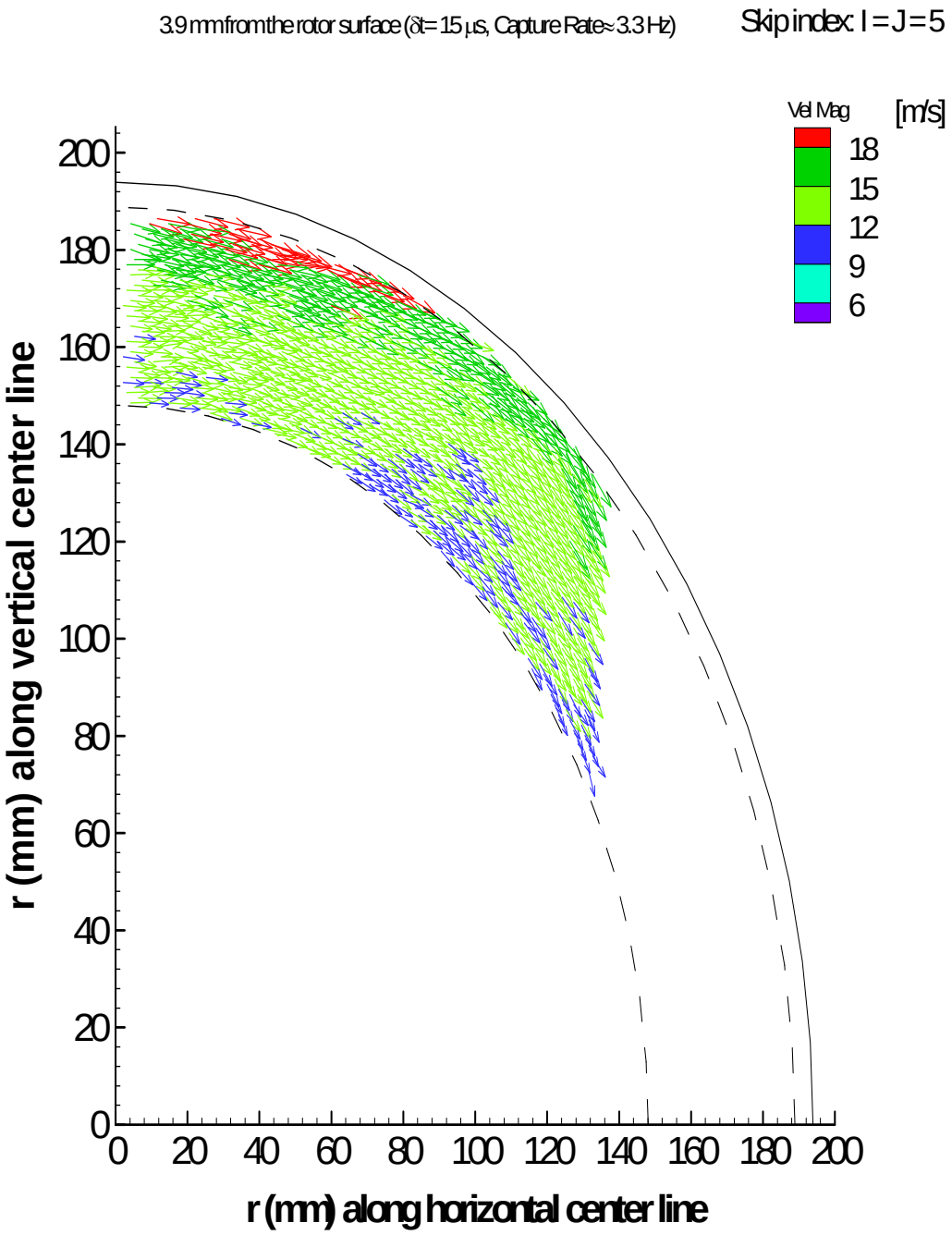

Fig. 3.19 An instantaneous fluid velocity vector map at x/s = 0.792 for Re_{φ}= 5.26×10^{5}, Re_{vax}= 7.12×10^{4}, c_w= 2465

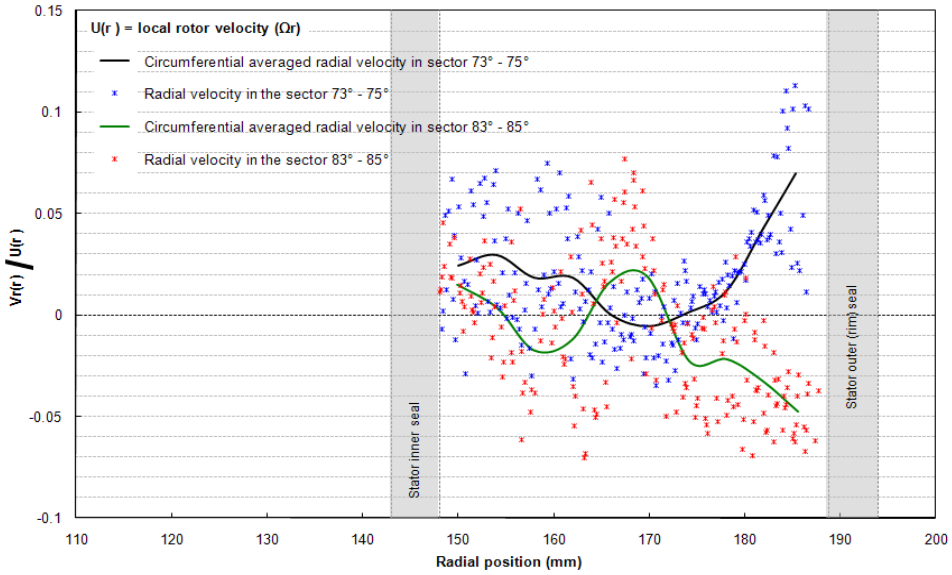

Fig. 3.20 Fluid instantaneous radial velocity over two different sectors for x/s = 0.792, $Re_{\varphi}= 5.26\times10^{5}$, $Re_{vax}= 7.12\times10^{4}$, $c_w= 2465$

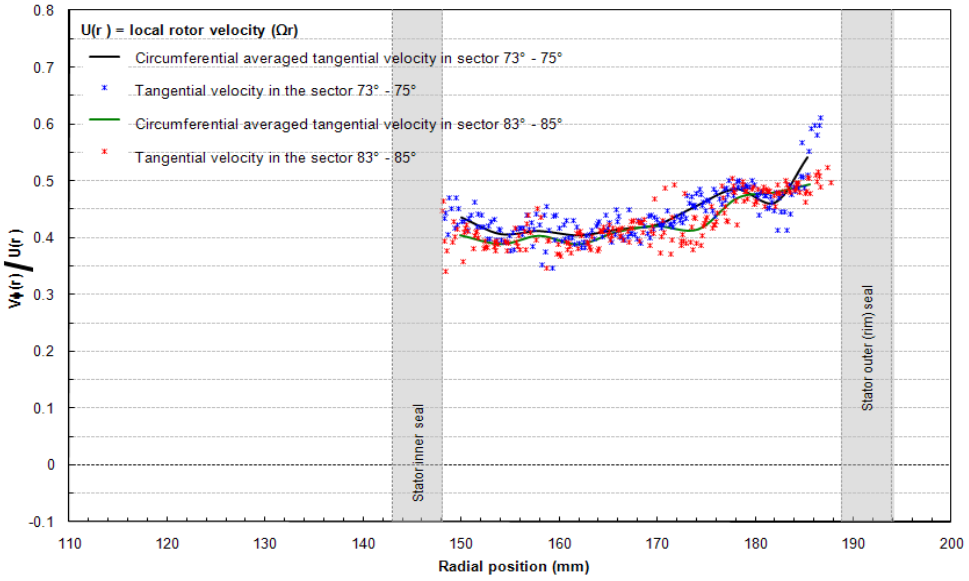

Fig. 3.21 Fluid instantaneous tangential velocity over two different sectors for x/s = 0.792, $Re_{\varphi}= 5.26\times10^{5}$, $Re_{vax}= 7.12\times10^{4}$, $c_w= 2465$

Chapter 4

CONCLUDING REMARKS

We have described experimental measurements of time-average static pressure field, time-average ingestion of main air, and instantaneous as well as ensemble-average fluid velocity field in the aft rotor-stator disk cavity of a model 1.5-stage axial-flow turbine. The measurements were done over ranges of mainstream and rotor speeds, and several purge air flows. The rotor disk was equipped with blades and the aft stator was equipped with vanes. It also included inlet vanes upstream of the rotor blades that formed along with the rotor blades the stage 1 main gas path. Rim seals with radial clearance and axial overlap were installed on the rotor disk and aft stator rims. An inner labyrinth seal divided the disk cavity into an inner cavity and an outer rim cavity.

Static-pressure readings were taken at: (i) seven radial locations on the stator surface, (ii) three axial positions on the outer shroud downstream of the rotor blades and (iii) on the outer shroud 3 mm downstream of stage 1 vanes. The pressure on the stator surface dropped by a significant amount across the labyrinth seal and then increased radially outward in the rim cavity. The pressure drop across the labyrinth seal increased with purge air flow rate. Circumferential periodicity in pressure that followed the vane pitch (both front and aft) was observed at the outer shroud downstream of the stage 1 vanes as well as the rotor blades. The periodic distribution also shifts in phase in the stream-wise direction.

Seal effectiveness distribution was measured at the stator surface in the aft disk cavity. The inner cavity was completely sealed off from main gas ingestion at

the higher purge flow rates. However, significant ingestion still occurred in the rim cavity. Ingestion was higher in the higher main flow, higher rotor speed experiments at the same purge air flow.

The ensemble-averaged velocity maps in the aft rim cavity showed that the tangential velocity was higher near the rotor disk compared to near the stator. The radial velocity was low throughout the rim cavity. In the instantaneous velocity maps, large fluctuations were seen in the radial velocity. In different circumferential sectors, the fluid radial velocity could be predominantly positive or negative.

REFERENCES

Abe, T., Kikuchi, J., and Takeuchi, H., 1979, "An Investigation of Turbine Disk and Cooling," 13th CIMAC Congress, Vienna.

Rabs, M., Benra, A. F., Dohmen, J. H., and Schneider, O., 2009, "Investigation of Flow Instabilities near the Rim Cavity of a 1.5 Stage Gas Turbine", ASME Paper No. GT2009-59965

Bohn, D., Rudzinski, B., Surken, N., and Gartner, W., 1999, "Influence of Rim Seal Geometry on Hot Gas Ingestion Into the Upstream Cavity of an Axial Turbine Stage," ASME Paper 99-GT-248.

Bohn, D., Rudzinski, B., Surken, N., and Gartner, W., 2000, "Experimental and Numerical Investigations of the Influence of Rotor Blades on Hot Gas Ingestion into the Upstream Cavity of an Axial Turbine Stage," ASME Paper 00-GT-284.

Cao, C., Chew, J.W., Millington, P.R., and Hogg, S.I., 2003, "Interaction of Rim Seal and Annulus Flows in an Axial Flow Turbine," ASME Paper GT-2003-38368.

Chew, J. W., Green, T, and Turner, A. B., 1994, "Rim Sealing of Rotor-Stator Wheelspaces in the Presence of External Flow," ASME Paper 94-GT-126.

Daily, J.W. and Nece, R.E., 1960, "Chamber Dimension Effects on Induced Flow and Frictional Resistance of Enclosed Rotating Disk," *ASME Journal of Basic Engineering*, Vol. 82, pp. 217-232.

Bohn, D. E., Decker, A., and Ohlendorf, N., 2006, "Influence of Radial and Axial Rim Seal Geometry on Hot Gas Ingestion into the Upstream Cavity of a 1.5 Stage Turbine", ASME Paper No. GT2006-90453

D, Narzary., Roy, R.P., Feng, J., 2005, "Ingestion into a Rotor-Stator Disk Cavity with Single- and Double-Rim Seals," AIAA Paper 2005-3982.

Jakoby, R., Zierer, T., Klas, L., and Larsson, J., deVito, L., Bohn, E. D., Funcke, J and Decker, A., 2004, "Numerical simulation of the Unsteady Flow Field in an Axial Gas Turbine Rim Seal Configuration," ASME Paper GT2004-53829

Gallier, K.D., Lawless, P.B., and Fleeter, S., 2000, "Investigation of Seal Purge Flow Effects on the Hub Flow Field in a Turbine Stage Using Particle Image Velocimetry," AIAA Paper 2000-3370.

Gentilhomme, O., Hills, N.J., Chew, J.W., and Turner, A.B., 2002, “Measurement and Analysis of Ingestion through a Turbine Rim Seal,” ASME Paper GT-2002-30481.

Green, T. and Turner, A. B., 1994, “Ingestion into the Upstream Wheelspace of an Axial Turbine Stage,” *ASME Journal of Turbomachinery*, Vol. 116, pp. 327-332.

Bohn, D. E., Decker, A., Ma, H., and Wolff, M., 2003, " Influence of Sealing Air Mass Flow on the Velocity Distribution In and Inside the Rim Seal of the Upstream Cavity of a 1.5 Stage Turbine", ASME Paper No. GT2003-38459

Owen, J.M. and Rogers, R.H., 1989, Flow and Heat Transfer in Rotating-Disc Systems. Vol. I: Rotor-Stator Systems, Research Studies Press, Taunton, United Kingdom.

Brodersen, S., Metzger D. E., Fernando H. J. S., 1996, “Flows Generated by the Impingement of a Jet on a Rotating Surface: Part I – Basic Flow Patterns”, *Journal of Fluids Engineering*, vol.118, 61-67.

Phadke, U. P. and Owen, J. M., 1988, “Aerodynamic Aspects of the Sealing of Gas-Turbine Rotor-Stator Systems, Part 3: The Effect of Nonaxisymmetric External Flow on Seal Performance,” *International Journal of Heat and Fluid Flow*, Vol. 9(2), pp. 113-117.

Roy, R.P., Agarwal, V., Devasenathipathy, S., He, J., Kim, Y. W., and Howe, J., 1997, “A Study of the Flow Field and Convective Heat Transfer in a Model Rotor-Stator Cavity,” *Experimental Methods in Heat Transfer*, HTD-Vol. 353, pp. 97-107, ASME Winter Annual Mtg., Dallas.

Roy, R.P., Devasenathipathy, S., Xu, G., and Zhao, Y., 1999, “A Study of the Flow Field in a Model Rotor-Stator Disk Cavity,” ASME Paper 99-GT-246.

Roy, R.P., Xu, G., and Feng, J., 2000, “Study of Main-stream Gas Ingestion in a Rotor-Stator Disk Cavity,” AIAA Paper 2000-3372.

Roy, R.P., Xu, G., Feng, J. and Kang, S., 2001, “Pressure Field and Main Stream Gas Ingestion in Rotor Stator Disk Cavity,” ASME Paper 2001-GT-564.

Roy, R.P., Feng, J., Narzary, D., and Paolillo, R.E., 2005, “Experiment on Gas Ingestion Through Axial-Flow Turbine Rim Seals,” *ASME Journal of Engineering for Gas Turbines and Power*, Vol. 127, pp. 573-582